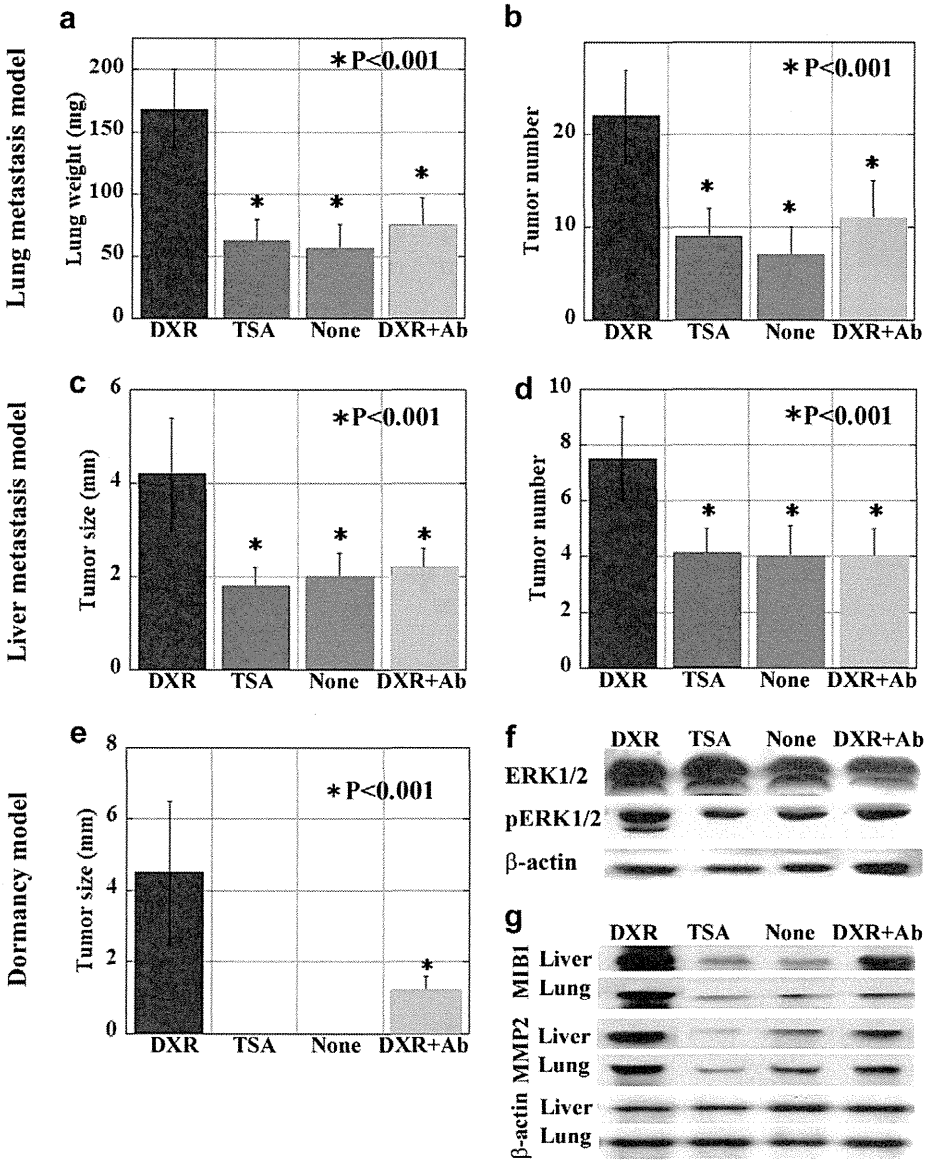

Fig. 5. Effect of cell death induction on metastasis of remnant cancer cells. CT26 cells were inoculated in the tail vein (for lung metastasis) or the spleen (liver metastasis) on day 6. doxorubicin (DXR) or trichostatin A (TSA) was injected into subcutaneous tumours on day 8. Metastasis was assessed on day 28. Anti-HMGB1 (Ab) antibody was administered on days 8 and 9. (a and b) Lung weight and number of metastatic foci of the lung. (c and d) Size and number of metastatic foci of the liver. (e) In an linoleic acid (LA)-induced dormancy model, tumour formation by LA-induced quiescent cells inoculated into subcutaneous tissue was assessed on day 28. Error bars represent standard deviation (SD). (f) Phosphorylation of extracellular signal-regulated protein kinase (ERK1/2) in the original tumour examined by immunoblotting. (g) Protein levels of MIB1 and MMP2 were examined by immunoblotting. β-Actin was examined as a loading control.

In CT26 cells, HMGB1 treatment increased IκB phosphorylation and nuclear translocation of the p65 subunit of NFκB, indicating activation of NFκB (Fig. 6f). However, RAGE knockdown inhibited HMGB1-induced NFκB activation at a more pronounced level than TLR4 knockdown did. Dual knockdown of RAGE and TLR4 resulted in total inhibition of NFκB activation by HMGB1 (Fig. 6d–g).

4. Discussion

Anti-cancer chemotherapy induces cell death in cancer cells via both necrotic and apoptotic mechanisms. Necrotic cell death permits the release of HMGB1 by loosening the nucleus.[2] Indeed, our data confirmed that necrosis inducers increase HMGB1 concentration in the CM. In contrast, the condensed nucleus found in apoptotic cells prevents the release of HMGB1. Similarly, we showed that an apoptosis inducer did not increase HMGB1 concentration in the CM. This difference in HMGB1 concentration was also observed in a mouse model; treatment of CT26 tumours with the necrosis inducer, but not the apoptosis inducer, increased serum HMGB1 levels.

HMGB1 is known to act as a growth factor for cancer cells,[9,16,17] because HMGB1 activates mitogen-acti-

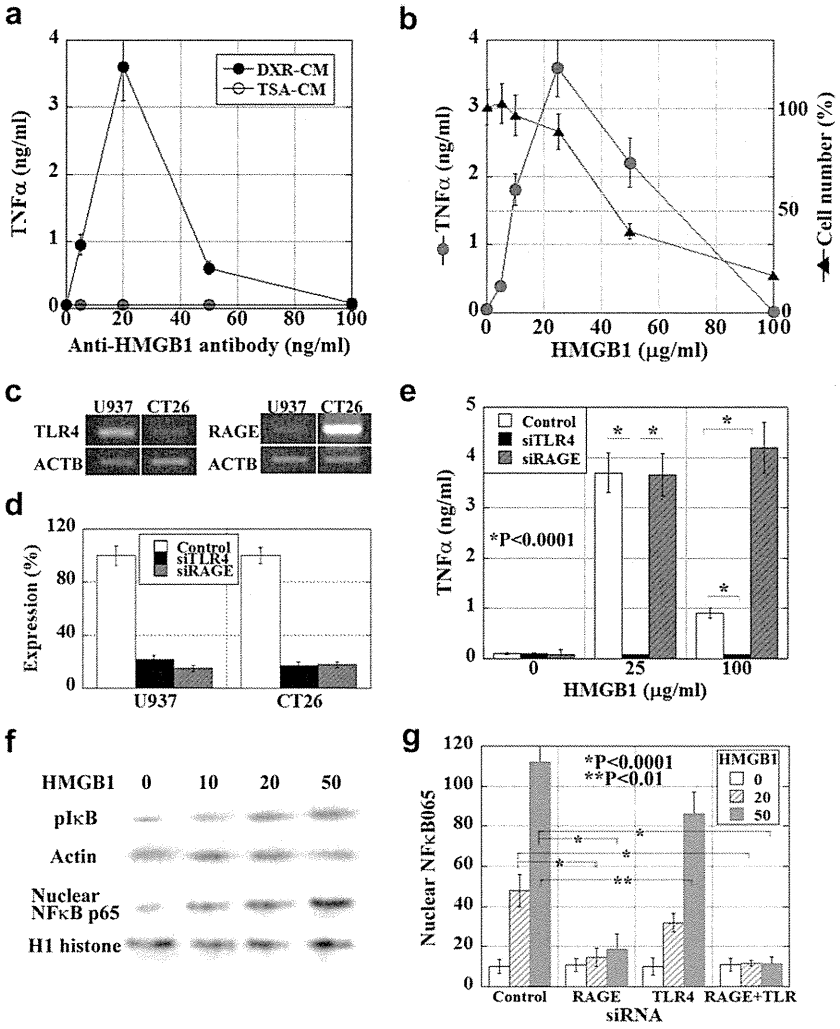

Fig. 6. Effect of HMGB1 on innate immunity and cancer survival. (a) U937 human monocytic leukaemia cells were incubated with CT26 cell culture medium (CM) treated with doxorubicin (DXR-CM) or trichostatin A (TSA) (TSA-CM), and HMGB1 was neutralised by an anti-HMGB1 antibody. TNF-α concentration in the CM was determined by enzyme-linked immunosorbent assay (ELISA). (b) U937 cells were treated with HMGB1, and cell number and CM TNF-α concentration were examined. (c) Expression of RAGE and TLR4 in U937 and CT26 cells was determined by reverse transcription-polymerase chain reaction (RT-PCR). (d) Effect of Small interfering RNA (siRNA) directed against RAGE and TLR4 on the expression of RAGE and TLR4 in U937 and CT26 cells. (e) Effect of knockdown of RAGE or TLR4 on TNF-α secretion by U937 cells. (f) Levels of phosphorylated IκB and nuclear NFκB p65 were examined by immunoblotting. Actin and H1 histone levels served as internal controls. (g) Effect of siRNA directed against RAGE and TLR4 on the levels of nuclear NFκB p65 in CT26 cells. Error bars represent standard deviation (SD).

vated protein kinase, and thereby enhances proliferation and invasion via activation of the RAGE receptor.[9,30] HMGB1 also activates mammalian target of rapamycin (mTOR) to enhance cancer cell survival.[31] HMGB1 acts as an inflammatory cytokine and as a suppressor of monocyte lineages, including lymph sinus macrophages, liver Kupffer cells and dendritic cells.[23,32–34] Furthermore, HMGB1 induces apoptosis in monocyte lineages, and this causes a reduction of anti-cancer immunity and an increase in the metastatic capacity of cancer cells.

Paradoxically, our data showed increased growth of remnant cancer cells and metastasis to the liver and lung in the necrosis inducer-treated mice. In contrast, this increase of tumour regrowth and metastasis was not found in the mice treated with an apoptosis inducer. Moreover, treatment with anti-HMGB1 antibody abrogated the increase of tumour regrowth and metastasis.

We previously reported that LA induces quiescence of cancer cells by the long-term treatment.[13] Furthermore, quiescent cancer cells adopt a dormant status in inoculated mice. Our data showed that induction of necrosis in a visible tumour activated LA-induced dormant cancer cells inoculated in the contralateral side of the back. In contrast, treatment with an apoptosis inducer did not activate the dormant cells. The mechanisms responsible for induction and breakage of the cancer dormancy are still unclear. However, our results suggest that HMGB1 released from necrotic cells by chemotherapy results in a dormancy break of hidden cancer cells.

Recently, HMGB1 has been shown to present DNA to TLRs to activate innate immunity.[6,7] This suggests that HMGB1 is capable of enhancing anti-cancer immunity; however, high levels of HMGB1 suppress monocyte lineages, thereby inhibiting anti-cancer immunity.

From our findings, we consider that apoptosis inducers are important for anti-cancer chemotherapy. Chemotherapy using necrosis inducers can lead to obvious reduction of tumours by necrosis; however, it may enhance regrowth and metastasis of cancer cells that have survived treatment, and activate scattered cancer cells that are in a dormant status. Alternatively, HMGB1 released from necrotic cancer cells may activate the innate immune system to promote host anti-cancer immunity. Thus, the role of chemotherapy-associated HMGB1 is thought to depend on the balance of these opposing effects of HMGB1. To confirm it, we examined the effect of HMGB1 on TNF-α secretion in U937 macrophages and NFκB activation in CT26 colon cancer cells. Our results suggest that RAGE-related HMGB1 effects are cancer activated and immunosuppressive. RAGE activation in CT26 cells induced NFκB activation, which enhances cancer cell survival. In contrast, RAGE activation in U937 cells reduced cell numbers and inhibited TNF-α secretion. RAGE activation induces apoptosis of U937 cells via c-Jun N-terminal kinase phosphorylation.[23] In contrast to RAGE, TLR4-related HMGB1 activated the immune system. TLR4 activation by HMGB1 induced TNF-α secretion in U937 cells, whereas TLR4 showed a restricted effect on NFκB activation in CT26 cells. These findings suggest that RAGE suppression is effective in avoiding regrowth and metastasis of cancer cells by necrosis-related HMGB1 in chemotherapy.

Our results suggest that to avoid cancer reactivation by HMGB1 released from necrotic cancer cells, it may be important to use apoptosis inducers as an alternative to necrosis inducers, or target RAGE by using necrosis inducers. Recently, a number of RAGE-targeting methods have been proposed.[1] Such proposals may be considered for future chemotherapy protocols, to establish more effective immunogenic chemotherapy.[7]

Conflict of interest statement

We declare that there is not any Financial Support or Relationships which may pose a conflict of interest in the contents of the submitted manuscript. All authors have approved the comments.

Acknowledgments

This work was supported in part by Grant-in-Aid for Scientific Research from Japan Society for the Promotion of Science, Japan, and Grant-in-Aid for Scientific Research from Ministry of Health, Labour and Welfare, Japan.

References

1. Ohmori H, Luo Y, Kuniyasu H. Non-histone nuclear factor HMGB1 as a therapeutic target in colorectal cancer. *Expert Opin Ther Targets* 2011;**15**(2):183–93.
2. Scaffidi P, Misteli T, Bianchi ME. Release of chromatin protein HMGB1 by necrotic cells triggers inflammation. *Nature* 2002;**418**(6894):191–5.
3. Lee KL, Pentecost BT, D'Anna JA, Tobey RA, Gurley LR, Dixon GH. Characterization of cDNA sequences corresponding to three distinct HMG-1 mRNA species in line CHO Chinese hamster cells and cell cycle expression of the HMG-1 gene. *Nucleic Acids Res* 1987;**15**:5051–68.
4. Rauvala H, Pihlaskari R. Isolation and some characteristics of an adhesive factor of brain that enhances neurite outgrowth in central neurons. *J Biol Chem* 1987;**262**:16625–35.
5. Parkkinen J, Raulo E, Merenmies J, et al. Amphoterin, the 30-kDa protein in a family of HMG1-type polypeptides. Enhanced expression in transformed cells, leading edge localization, and interactions with plasminogen activation. *J Biol Chem* 1993;**268**:685–91.
6. Stros M. HMGB proteins: interactions with DNA and chromatin. *Biochim Biophys Acta* 2010;**1799**(1–2):101–13.
7. Tesniere A, Apetoh L, Ghiringhelli F, et al. Immunogenic cancer cell death: a key-lock paradigm. *Curr Opin Immunol* 2008;**20**(5):504–11.
8. Taguchi A, Blood DC, del Toro G, et al. Blockade of RAGE-amphoterin signalling suppresses tumour growth and metastases. *Nature* 2000;**405**(6784):354–60.
9. Czura CJ, Wang H, Tracey KJ. Dual roles for HMGB1: DNA binding and cytokine. *J Endotoxin Res* 2001;**7**(4):315–21.
10. Degryse B, Bonaldi T, Scaffidi P, et al. The high mobility group (HMG) boxes of the nuclear protein HMG1 induce chemotaxis and cytoskeleton reorganization in rat smooth muscle cells. *J Cell Biol* 2001;**152**(6):1197–206.
11. Sasahira T, Sasaki T, Kuniyasu H. Interleukin-15 and transforming growth factor a are associated with depletion of tumor-associated macrophages in colon cancer. *J Exp Clin Cancer Res* 2005;**24**(1):69–74.
12. Kuniyasu H, Chihara Y, Kondo H, Ohmori H, Ukai R. Amphoterin induction in prostatic stromal cells by androgen deprivation is associated with metastatic prostate cancer. *Oncol Rep* 2003;**10**(6):1863–8.
13. Ohmori H, Sasahira T, Fujii K, Luo Y, Shimomoto T, Kuniyasu H. Linoleic acid-induced growth suppression induces quiescent cancer cell nests in nude mice. *Pathobiology* 2008;**75**(4):226–32.
14. Fujii K, Luo Y, Sasahira T, Denda A, Ohmori H, Kuniyasu H. Co-treatment with deoxycholic acid and azoxymethane accelerates the secretion of HMGB1 in IEC6 intestinal epithelial cells. *Cell Prolif* 2009;**42**(5):701–9.
15. Yamamoto K, Kitayama W, Denda A, Sasahira T, Kuniyasu H, Kirita T. Expression of receptor for advanced glycation end products during rat tongue carcinogenesis by 4-nitroquinoline 1-oxide and effect of a selective cyclooxygenase-2 inhibitor, etodolac. *Pathobiology* 2006;**73**(6):317–24.
16. Kuniyasu H, Oue N, Wakikawa A, et al. Expression of receptors for advanced glycation end-products (RAGE) is closely associated with the invasive and metastatic activity of gastric cancer. *J Pathol* 2002;**196**(2):163–70.
17. Kuniyasu H, Chihara Y, Takahashi T. Co-expression of receptor for advanced glycation end products and the ligand amphoterin associates closely with metastasis of colorectal cancer. *Oncol Rep* 2003;**10**(2):445–8.

18. Kuniyasu H, Chihara Y, Kondo H. Differential effects between amphoterin and advanced glycation end products on colon cancer cells. *Int J Cancer* 2003;**104**(6):722–7.
19. Pallier C, Scaffidi P, Chopineau-Proust S, et al. Association of chromatin proteins high mobility group box (HMGB) 1 and HMGB2 with mitotic chromosomes. *Mol Biol Cell* 2003;**14**(8):3414–26.
20. Travers AA. Priming the nucleosome: a role for HMGB proteins? *EMBO Rep* 2003;**4**(2):131–6.
21. Gardella S, Andrei C, Ferrera D, et al. The nuclear protein HMGB1 is secreted by monocytes via a non-classical, vesicle-mediated secretory pathway. *EMBO Rep* 2002;**3**(10):995–1001.
22. Apetoh L, Ghiringhelli F, Tesniere A, et al. Toll-like receptor 4-dependent contribution of the immune system to anticancer chemotherapy and radiotherapy. *Nat Med* 2007;**13**(9):1050–9.
23. Kuniyasu H, Yano S, Sasaki T, Sasahira T, Sone S, Ohmori H. Colon cancer cell-derived high mobility group 1/amphoterin induces growth inhibition and apoptosis in macrophages. *Am J Pathol* 2005;**166**(3):751–60.
24. Kuniyasu H, Yasui W, Shinohara H, et al. Induction of angiogenesis by hyperplastic colonic mucosa adjacent to colon cancer. *Am J Pathol* 2000;**157**(5):1523–35.
25. Sasaki T, Yoshida K, Shimura H, et al. Inhibitory effect of linoleic acid on transformation of IEC6 intestinal cells by in vitro azoxymethane treatment. *Int J Cancer* 2006;**118**(3):593–9.
26. Liu A, Fang H, Dirsch O, Jin H, Dahmen U. Oxidation of HMGB1 causes attenuation of its pro-inflammatory activity and occurs during liver ischemia and reperfusion. *PLoS One* 2012;**7**(4):e35379.
27. Tang D, Kang R, Cheh CW, et al. HMGB1 release and redox regulates autophagy and apoptosis in cancer cells. *Oncogene* 2010;**29**(38):5299–310.
28. Tang D, Kang R, Livesey KM, et al. Endogenous HMGB1 regulates autophagy. *J Cell Biol* 2010;**190**(5):881–92.
29. Ulloa L, Ochani M, Yang H, et al. Ethyl pyruvate prevents lethality in mice with established lethal sepsis and systemic inflammation. *Proc Natl Acad Sci U S A* 2002;**99**(19):12351–6.
30. Bhawal UK, Ozaki Y, Nishimura M, et al. Association of expression of receptor for advanced glycation end products and invasive activity of oral squamous cell carcinoma. *Oncology* 2005;**69**(3):246–55.
31. Kang R, Tang D, Schapiro NE, et al. The receptor for advanced glycation end products (RAGE) sustains autophagy and limits apoptosis, promoting pancreatic tumor cell survival. *Cell Death Differ* 2010;**17**(4):666–76.
32. Moriwaka Y, Luo Y, Ohmori H, et al. HMGB1 attenuates anti-metastatic defense of the lymph nodes in colorectal cancer. *Pathobiology* 2010;**77**(1):17–23.
33. Luo Y, Ohmori H, Fujii K, et al. HMGB1 attenuates anti-metastatic defence of the liver in colorectal cancer. *Eur J Cancer* 2010;**46**(4):791–9.
34. Kusume A, Sasahira T, Luo Y, et al. Suppression of dendritic cells by HMGB1 is associated with lymph node metastasis of human colon cancer. *Pathobiology* 2009;**76**(4):155–62.

PLOS | ONE

In Vivo Imaging of Enteric Neurogenesis in the Deep Tissue of Mouse Small Intestine

Kei Goto[1,2], Go Kato[3], Isao Kawahara[1,2], Yi Luo[2], Koji Obata[1], Hiromi Misawa[1], Tatsuya Ishikawa[3], Hiroki Kuniyasu[2], Junich Nabekura[3], Miyako Takaki[1,2]*

1 Department of Physiology II, Nara Medical University, School of Medicine, Kashihara, Nara, Japan, **2** Department of Molecular Pathology, Nara Medical University, School of Medicine, Kashihara, Nara, Japan, **3** Division of Homeostatic Development, Department of Developmental Physiology, National Institute for Physiological Sciences, Okazaki, Aichi, Japan

Abstract

One of the challenges of using imaging techniques as a tool to study cellular physiology has been the inability to resolve structures that are not located near the surface of the preparation. Nonlinear optical microscopy, in particular two photon-excited fluorescence microscopy (2PM), has overcome this limitation, providing deeper optical penetration (several hundred μm) in ex vivo and in vivo preparations. We have used this approach in the gut to achieve the first in vivo imaging of enteric neurons and nerve fibers in the mucosa, submucosa, submucosal and myenteric plexuses, and circular and longitudinal muscles of the small intestine in H-line: Thy1 promoter GFP mice. Moreover, we obtained clear three-dimensional imaging of enteric neurons that were newly generated after gut transection and reanastomosis. Neurogenesis was promoted by oral application of the 5-HT_4-receptor agonist, mosapride citrate (MOS). The number of newly generated neurons observed in mice treated with MOS for one week was 421±89 per 864,900 μm^2 (n = 5), which was significantly greater than that observed in preparations treated with MOS plus an antagonist (113±76 per 864,900 μm^2) or in 4 week vehicle controls (100±34 per 864,900 μm^2) (n = 4 both). Most neurons were located within 100 μm of the surface. These results confirm that activation of enteric neural 5-HT_4-receptor by MOS promotes formation of new enteric neurons. We conclude that in vivo 2PM imaging made it possible to perform high-resolution deep imaging of the living mouse whole gut and reveal formation of new enteric neurons promoted by 5-HT_4-receptor activation.

Citation: Goto K, Kato G, Kawahara I, Luo Y, Obata K, et al. (2013) In Vivo Imaging of Enteric Neurogenesis in the Deep Tissue of Mouse Small Intestine. PLoS ONE 8(1): e54814. doi:10.1371/journal.pone.0054814

Editor: Yvette Tache, University of California Los Angeles, United States of America

Received July 23, 2012; **Accepted** December 17, 2012; **Published** January 31, 2013

Funding: This study was supported by the Cooperative Study Program of National Institute for Physiological Sciences. This work was supported by Grants-in-aid for Scientific Research (20659210, 23390330, 24650325 for M.T. and 23591969 for H.M.) from the Ministry of Education, Science, Sports and Culture of Japan. The funders had no role in study design, data collection and analysis, decision to publish, or preparation of the manuscript.

Competing Interests: The authors have declared that no competing interests exist.

* E-mail: mtakaki@naramed-u.ac.jp

Introduction

Activation of enteric neural 5-HT_4-receptors by mosapride citrate (MOS) promotes the reconstruction of an enteric neural circuit injured after surgery, leading to the recovery of the 'defecation reflex' [1,2] in the distal gut of guinea pigs [3]. This neural plasticity involves neural stem cells [3]. Recently, we also revealed that MOS enhances neural network formation in gut-like organs differentiated from mouse embryonic stem cells [4]. Other 5-HT_4 receptor agonists also increase neuronal numbers and length of neurites in enteric neurons developing in vitro from immunoselected neural crest-derived precursors [5]. 5-HT_4 receptor-mediated neuroprotection and neurogenesis has also been demonstrated in the enteric nervous system of adult mice [6]. We therefore explored the ability of MOS to promote the generation of new enteric neurons at resected sites of the mouse small intestine *in vivo*. The new neurons are typically located in regions of granulation tissue, which is new connective tissue formed by growth of fibroblasts and blood capillaries into injured tissue after transection and reanastomosis of the gut.

Unfortunately, it is impossible for traditional fluorescence microscopy including confocal microscopy to perform high-resolution deep imaging of the 300–400 μm thick granulation tissue that is formed during the tissue repairing process at the anastomotic site after transection of the gut. Even in in vitro whole mount preparations, in which the mucosal, submucosal and circular muscle layers were removed, imaging of newly formed neurons and axons is severely limited. Nonlinear optical microscopy, in particular two photon-excited fluorescence microscopy, offers a means to overcome this limitation by providing enhanced optical penetration. Two-photon microscopy (2PM) allows cellular imaging several hundred microns deep in various organs of living animals and ex vivo specimens [7].

In the present study, we employed 2PM to obtain 3-dimensional reconstructions of impaired enteric neural circuits within the thick granulation tissue in the ileum of Thy1-GFP mice [8], in which the GFP is expressed in the cytoplasm of enteric neurons. Although in vivo imaging of the muscularis propria and myenteric neurons with probe-based confocal laser endomicroscopy in porcine models has been recently reported [9], we obtained the first ever (deleted) clear three-dimensional imaging of newly generated enteric neurons within the thick granulation tissue at the anastomosis, indicating that 2PM allows enteric neural imaging several hundred microns deep in the gut of the living mouse. The most critical challenge was to suppress movement artifacts to allow

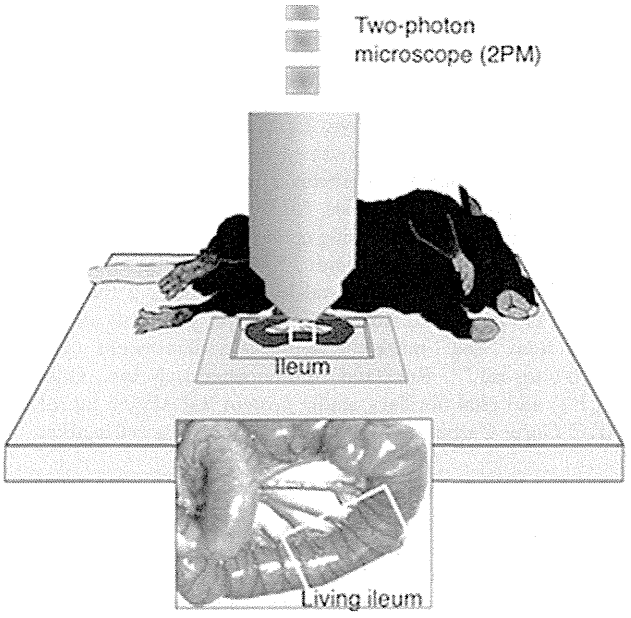

Figure 1. Depiction of the experimental approach for *in vivo* imaging of the intestine.
doi:10.1371/journal.pone.0054814.g001

for microscopy in the living gut. In addition, we tested whether activation of enteric neural 5-HT_4-receptors by MOS promotes reconstruction of an enteric neural circuit injured after the surgery as has been demonstrated in the lower gut [3].

Materials and Methods

Description and Preparation of Transgenic Mice Used for Imaging

All relevant experimental protocols were approved by the Ethics Review Committee for Animal Experimentation of the National Institutes for Physiological Sciences (permission number: 11A114). We used a transgenic mouse, based on the C57BL/6 strain, with sparse expression of cytoplasmic GFP in thalamic and cortical pyramidal neurons (Thy1 promoter GFP mouse, H-line) [8]. In preliminary studies, we confirmed expression of cytoplasmic GFP in enteric neurons. Transgenic mice, at 8–12 weeks after birth, were anesthetized with an intraperitoneal injection of Nembutal (50 mg kg^{-1}) and the abdomen was opened by a lower midline laparotomy. This approach spared vascular perfusion and maintained extrinsic inputs from the mesenteric nerves. The ileum was transected 5–6 cm from ileo-cecal sphincter and an end-to-end one-layer anastomosis was performed. Body temperature was maintained at 36–37°C using a heating pad. After recovery from the surgical procedure, mouse daily drank 0.1% DMSO vehicle solution (n = 5), MOS (100 μM) in vehicle (n = 6), or a selective 5-HT_4-blocker for oral application, SB-207266 (SB: 10–50 μM) [10] plus MOS (100 μM) in vehicle (n = 4) for 1 week (with the beginning two days fasting and the ending five days feeding ad libitum). In addition, vehicle controls were maintained for 4 weeks (n = 4) with the beginning two days fasting and the ending twenty-six days feeding.

In vivo Two-photon Microscopy

Seven days after the surgery, the mice were anesthetized with Nembutal (50 mg kg^{-1}) for in vivo microscopy. Body temperature was maintained at 36–37°C using a disposable pocket body warmer. Additional Nembutal was administered as needed. The depth of anesthesia was assessed by monitoring respiration rate and vibrissae movements. The abdomen was opened by a lower midline laparotomy and the surgical site of the ileum was fixed into the chamber for 2PM without disturbance of blood supply (**Figure 1**). To suppress ileal motility for microscopy, the preparation was pinned in place and papaverine (1 mM; 0.1–

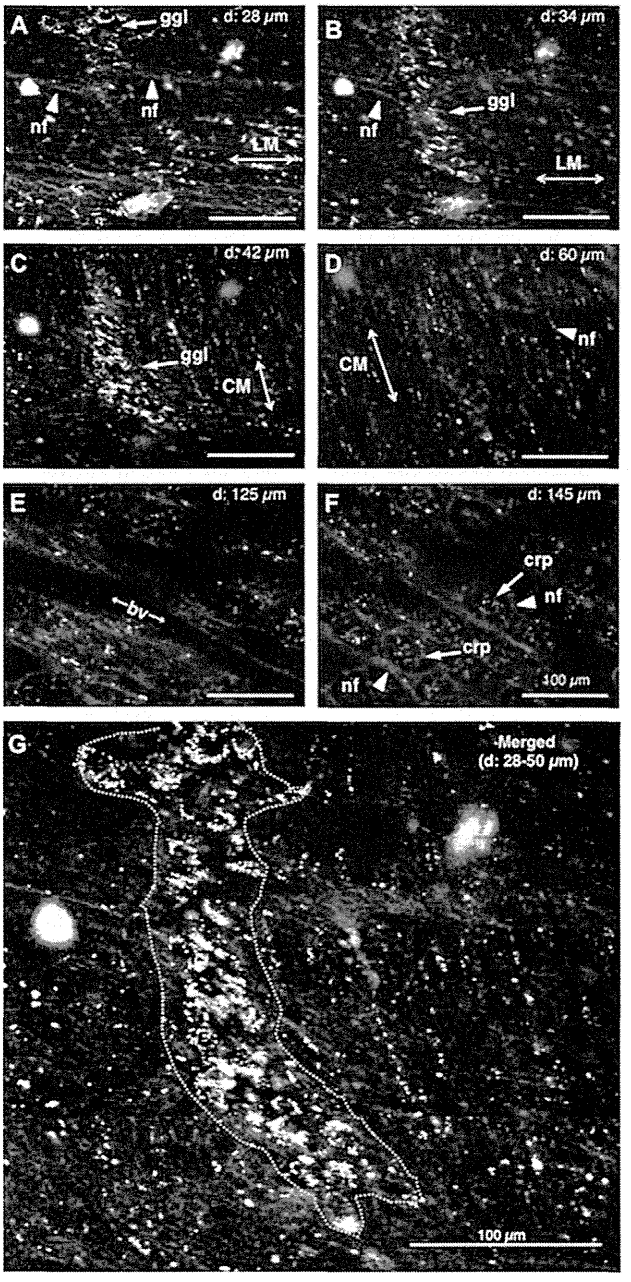

Figure 2. In vivo imaging of enteric neurons in the terminal ileum of an intact Thy1-GFP mouse. ***A.*** 28 μm deep to the serosal surface. ***B.*** 34 μm deep to the serosal surface. ***C.*** 42 μm deep to the serosal surface. ***D.*** 60 μm deep to the serosal surface. ***E.*** 125 μm deep to the serosal surface. ***F.*** 145 μm deep to the serosal surface. ***G.*** Merge of 28–50 μm deep images into a single image. Yellow arrows indicate ganglion (ggl) in ***A–C***, and yellow arrowheads indicate nerve fibers in ***A, B, D*** and ***F***, respectively. LM: longitudinal muscle. CM: circular muscle. bv: blood vessel. crp: crypt. Cal bar, 100 μm.
doi:10.1371/journal.pone.0054814.g002

0.2 ml) was injected intraluminally. Images were obtained at the rate of 2.711 sec frame^{-1}. GFP-labeled structures were imaged by a 2PM customized for in vivo imaging (FV1000-MPE, Olympus, Tokyo) using a water-immersion objective lens (40X, NA0.8, Olympus) at zoom of 1.0. A Ti-sapphire laser (MaiTai Hp, Spectral Physics, Mountain View, CA, USA) was tuned to the excitation wavelength for GFP (950 nm). The z-stack images consisted of 100–300 optical sections and were taken 1 μm apart (within 400 μm of the serosal surface). The photomultiplier tube setting and excitation power (~50 mW) remained constant during imaging. Under these conditions, the neurons seem to be still healthy after imaging (personal communication from Dr. Go Kato).

Immunohistochemical Imaging by Confocal Microscope

Following in vivo imaging, the animals were euthanized by administration of excessive dose of Nembutal, and whole mount preparations of the anastomosed regions of ileum were fixed in 4% paraformaldehyde (4°C, overnight) or 99.5% acetone (4°C, 1 hr) to detect neurofilament (NF). Thereafter, the mucosa and submucosa and granulation tissue were carefully removed, and following a 30 min wash in PBS (0.01–0.1 mol L^{-1}, pH 7.4) the preparations were incubated for 3–12 hrs at 4°C in 10% normal donkey serum in PBS containing 0.3% (v/v) Triton-X 100 (PBS-TX) to enhance penetration of antibodies. The preparations were then incubated for two days at 4°C with a rabbit polyclonal antiserum cocktail to label NF (clone 2F11, reacting with 70, 160 and 200 kDa proteins, 0.5 μg/ml; DAKO). NF immunoreactivity was detected using an Alexa Fluor 594-conjugated secondary antibody (Invitrogen Inc., Carisbad, CA). Tissues were examined with an OLYMPUS FV1000 (Tokyo, Japan) confocal microscope. Confocal images were constructed as digital composites of Z-series scans of 10–15 optical sections through a depth of 10–20 μm or 100–150 μm. Final images were produced with the FV10-ASW software application [Ver1.7] (OLYMPUS).

Immunohistochemistry of Sectioned Preparations

The rectum including an anastomotic site was fixed with 4% paraformaldehyde at 4°C, and embedded in paraffin. Consecutive 4 μm sections were cut from each block. Immunostaining was performed by treatment with pepsin (DAKO Corp., Carpinteria, CA, USA) for 20 min at room temperature for NF, DLX2, GFP and GFAP. After endogenous peroxidase blockade with 3% H_2O_2-methanol for 15 min, specimens were rinsed with PBS and incubated with a primary antibody diluted with Washing Solution (BioGenex, San Ramon, CA, USA) at room temperature for 2 hours. The specimens were rinsed with PBS and incubated at room temperature for 1 hour with secondary antibody conjugated to peroxidase diluted at 0.5 μg mL^{-1} (Medical & Biotechnological Laboratories Co., Ltd., Nagoya, Japan). The sections were then rinsed with PBS and color-developed by diaminobenzidine (DAB) solution (DAKO) and counterstained with Meyer's hematoxylin (Sigma Chemical Co., St. Louis, MO, USA). Antibodies used in primary reaction and the working concentrations were as followed: anti-NF (clone 2F11, reacting with 70, 160, and 200 kDa proteins, 0.5 μg mL^{-1}, DAKO), anti-distal less homeobox 2 (DLX2)(cat. ab18188, 0.5 μg mL^{-1}, Abcam Co, Tokyo, Japan) as an enteric neural stem cell marker, anti-green fluorescent protein (GFP)(0.5 μg mL^{-1}, Rockland Immunochemicals Inc., Gilbertsville, PA) and glial fibrillary acidic protein (GFAP)(0.5 μg mL^{-1}, DAKO Corp, Carpintaria, CA) as an enteric glia cell marker.

Detection of Regenerated Enteric Neurons

To identify neuronal cell proliferation, 5-bromo-2-deoxyuridine, BrdU (1 mg mL^{-1} solution; Sigma or NACALAI TESQUE, INC, Kyoto, Japan) was added to the drinking water containing MOS (100 μM) for 1–2 weeks for 6 animals. After rinsing in PBS, the specimens were pretreated with sodium chloride sodium citrate solution for 2 hrs at 65°C, followed by partial denaturation of double-stranded DNA with 2 mol L^{-1} HCl for 30 min at 37°C. To reveal BrdU, the sections were incubated with a rat monoclonal antibody raised against BrdU (Abcam Inc.) overnight at 4°C. The specimens were rinsed in 0.1 mol L^{-1} TE (pH 7.8) followed by routine immunohistochemistry.

Statistics

Multiple comparisons were performed by one-way analysis of variance (ANOVA) with post-hoc Bonferroni's test. A value of $p<0.05$ was considered statistically significant. All data are expressed as the mean ± S.D.

Results

In the current study, we obtained the first in vivo images of enteric neurons and nerve fibers in the mucosa, submucosa,

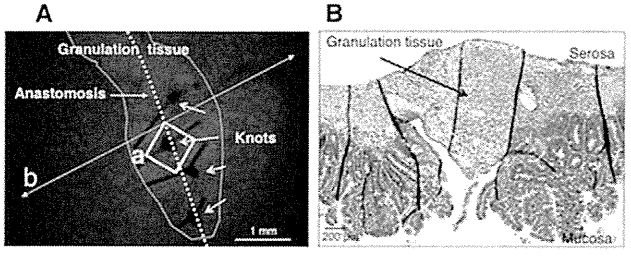

Figure 3. A stereomicroscopic image including the observed site shown in Figure 4. ***A.*** The thick granulation tissue at the anastomotic region in a mouse that was treated with MOS solution for 1 week after anastomosis surgery. An area in the square (**a**) corresponds to an area in the square (**a**) in **Figure 4**. ***B.*** A microscopic image of a longitudinal section, prepared following fixation, that was taken along the line (**b**) indicated in panel ***A***.
doi:10.1371/journal.pone.0054814.g003

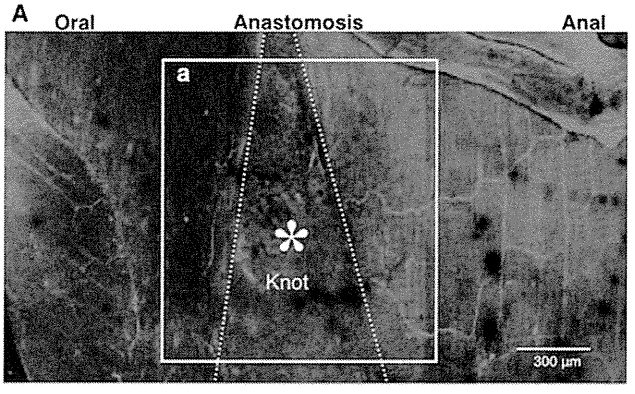

Figure 4. Immunohistochemical image for anti-neurofilament (NF) antibody of a whole mount preparation of the same intestine shown in Figure 5. *A–a* corresponds to Figure 5*A* (the image by 2PM). *, A knot of thread in the area between two-dotted lines indicates the anastomotic area. The granulation tissue was removed to allow for laser penetration. Normal myenteric plexus in the intact oral and anal sites are visible, but nerve cells and fibers are not visible in the anastomotic region because of the thickness of the anastomotic area.
doi:10.1371/journal.pone.0054814.g004

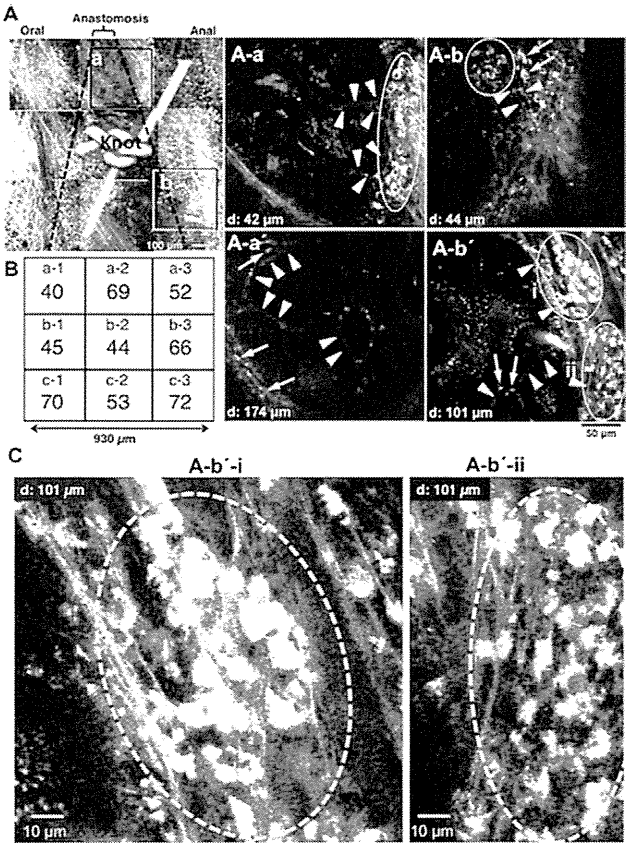

Figure 5. Images of anastomotic region of the terminal ileum in a MOS-treated mouse. The dotted lines indicates the anastomosis site. Around the knot of thread we obtained each image from 9 visual fields. ***A.*** Images stacked with Z axis to a total depth of 200–300 μm. ***A–a.*** image 42 μm deep to the serosa surface in area (***a***) in ***A***. ***A–a′.*** image 174 μm deep to the serosa surface in the same area (***a***) in ***A***. ***A–b.*** 44 μm deep to the serosa surface in area (***b***) in ***A***. ***A–b′.*** image 101 μm deep to the serosa surface in the same area (***b***) in ***A***. Arrows indicate nerve cells in ***A–a′***, ***b*** and ***b′***, and arrowheads indicate nerve fibers in ***A–a***, ***a′***, ***b*** and ***b′***, and circles indicate ganglion-like clusters of neurons in ***A–a***, ***b*** and ***b′***, respectively. ***B.*** Number of neurons in each field (size: 310 μm×310 μm) around the knot. ***C.*** Newborn nerve cells formed ganglion structures indicated by circles. These were enlarged from the images shown in ***A–b′–i*** and ***–ii.***

doi:10.1371/journal.pone.0054814.g005

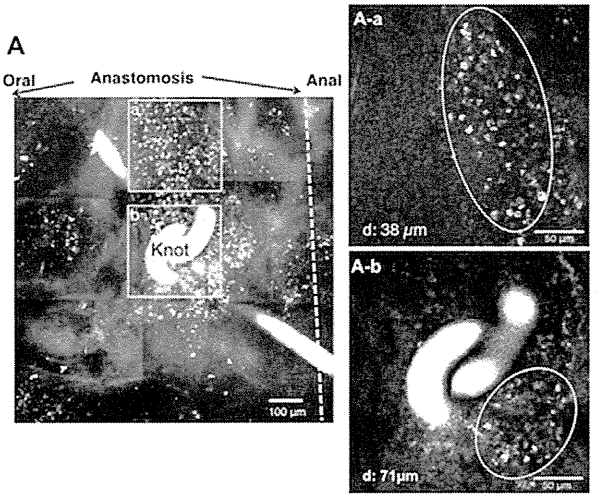

Figure 6. Images of anastomosis of the ileum in an SB-207266 (SB) plus MOS treated mouse. SB plus MOS treatment was performed for one week. ***A.*** Images stacked in the Z axis with a total depth of 200 - 300 μm. ***A–a.*** image 38 μm deep to the serosa surface in area (***a***) in ***A***. ***A–b.*** image 71 μm deep to the serosa surface in area (***b***) in ***A***. Circles indicate aggregates of small non-neuronal cells (***A–a*** and ***b***), respectively.

doi:10.1371/journal.pone.0054814.g006

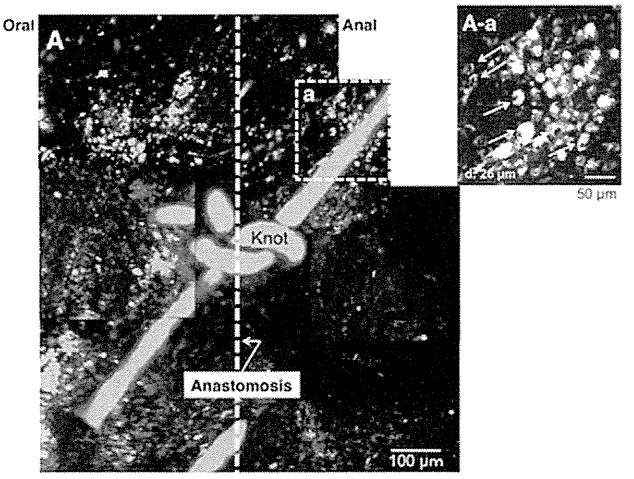

Figure 7. Images of around the suture knot at anastomosis of the ileum in DMSO treated mouse. Vehicle treatments were performed for 4 weeks. The dotted line indicates the anastomosis. ***A.*** Images stacked with Z axis up to a total depth of 151 - 201 μm. ***A–a.*** image 26 μm deep to the serosa surface close to the thread around the knot. A small number of neurons are visible.

doi:10.1371/journal.pone.0054814.g007

submucosal and myenteric plexuses, and circular and longitudinal muscles of the terminal ileum (**Figure 2**). We initially confirmed that enteric neurons could be imaged in vivo in the terminal ileum of an intact Thy1-GFP mouse (**Figure 2**). The normal mouse gut was rather thin, with a maximal thickness at myenteric ganglion level of 50 μm. Although images stacked with a Z-axis depth up to 50 μm showed low signal/background fluorescence intensity ratio, each image at depth of 28 μm–42 μm from serosa showed a single myenteric ganglion and longitudinal & circular muscle layers (**Figure 2*A–C***). Thicker images at depth of 60, 125 and 145 μm also showed nerve fibers in circular muscle layers, blood vessels and nerve fibers around crypts (Figure 2D–F), respectively. Living cells in a given ganglion were clearly observed in merged images at depth of 28 μm–50 μm (**Figure 2*G***).

A stereomicroscopic image demonstrating the thick granulation tissue at the anastomotic region in mouse treated with MOS solution for 1 week after surgical anastomosis is shown in **Figure 3*A***. However, under a stereomicroscopy no nerve cells or fibers were visible. A longitudinal section including the same granulation tissue indicates an obvious thickness of the tissue (**Figure 3*B***).

Using confocal imaging of the fixed whole mount preparation, no nerve cells or fibers were visible in the granulation tissue at the anastomosis, although intact myenteric plexus was visible in the intact area in a mouse treated with MOS solution for 1 week after surgery (**Figure 4**). The living ileum before fixation is shown in Figure 5.

In mice treated with MOS solution for 1 week after anastomosis, new ganglia-like structures and nerve fibers were

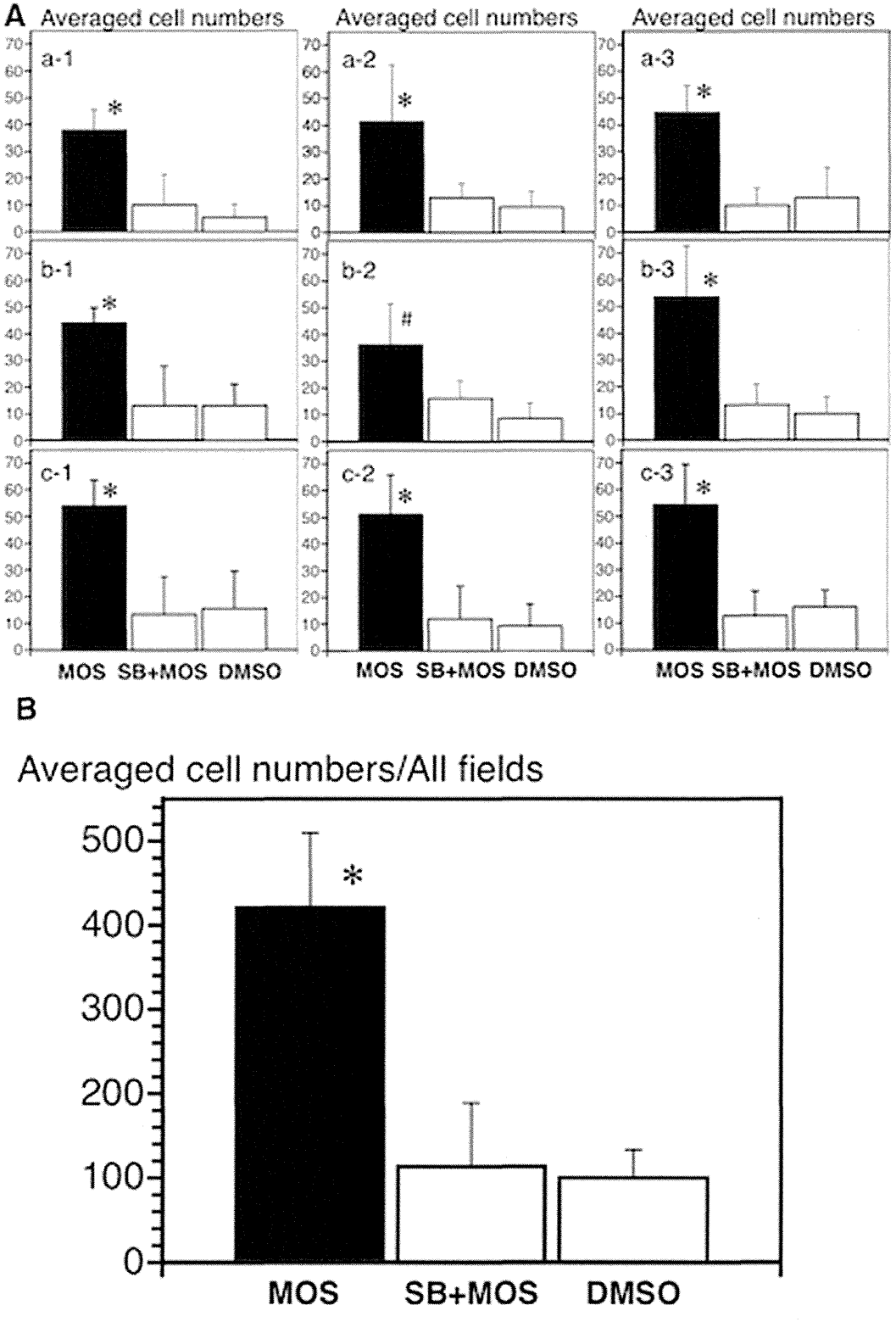

Figure 8. The average cell numbers in each of nine fields (A) and all fields (B) at the anastomosis. The comparison was performed among MOS (n = 5), SB+MOS (n = 4) and vehicle-treated (n = 4) mice. Each of the nine fields corresponds to that in Figure 5B. *, $P<0.05$ vs. SB+MOS and vehicle. #, $P<0.05$ vs. vehicle.
doi:10.1371/journal.pone.0054814.g008

observed by *in vivo* imaging of the thick granulation tissue at the anastomotic region of the living ileum (**Figure 5*A***). In sites both oral (**Figure 5*A–a* & *-a'***) and anal (**Figure 5*A–b* & *−b'***) to the anastomotic site, new ganglia-like structures packed with many of

newborn neurons and interganglionic nerve fibers were apparent in each image regardless of the depth from the serosa indicating that in the granulation tissue a new enteric neural network was being formed. The density of neurons observed within the anastomosis was 511 cells per 864,900 μm^2. The distribution of neurons was even in each nine field (from a−1 to c−3) (**Figure *5B***). **Figure 5*C*** clearly illustrates new neurons in two typical ganglion-like structures.

In mice treated with the 5-HT_4 antagonist, SB 207266 (SB) plus MOS solution for 1 week after anastomosis, no neurons or nerve fibers were observed in the anastomotic region (**Figure 6**), although aggregates of small cells (not neurons) were observed near the surface (**Figure 6*A–a* & *–b***). Thus, enteric neurogenesis was largely suppressed by simultaneous administration of the 5-HT_4 receptor blocker, SB along with MOS. Similar results were obtained with all 4 mice treated with MOS and SB.

Using confocal imaging of fixed, whole mount preparations, no nerve cells or fibers were visible in the granulation tissue at the anastomosis, although intact myenteric plexus was visible in the intact area in a mouse treated with SB and MOS solution for 1 week after surgery (data not shown).

Vehicle treated mice underwent in vivo imaging of the anastomotic region at 1 week (n = 5) and 4 weeks (n = 4) after ileum transection and re-anastomosis (**Figure 7**). One week after surgery, neither nerve bundles nor ganglia were visualized at the anastomosis. In contrast, 4 weeks after surgery, a small number of neurons were detected in one preparation (**Figure 7*A–a***). In the other three mice treated with vehicle for 4 weeks after surgery, no neurons were detected at any depth within the granulation tissue.

The average number of neurons observed amongst nine fields within the anastomosis in mice treated with MOS solution was significantly ($P<0.05$) larger than that in SB plus MOS treated mice (n = 4) or DMSO-treated mice (n = 4) after anastomosis (**Figure 8*A***). New neurons were observed without oral or anal and mesenteric or anti-mesenteric localizations in any of the three groups (**Figure 8*A***).

The average density of neurons observed in all fields within the anastomosis in mice treated with MOS solution was 421±89 per 864,900 μm^2 (n = 5), significantly ($P<0.05$) higher than SB plus MOS treated mice (113±76 per 864,900 μm^2; n = 4) or mice treated with vehicle (100±34 per 864,900 μm^2; n = 4) (Figure 8B). Moreover, the average number of neurons distributed at the anastomosis in MOS treated mice was about 5 cells per 10,000 μm^2, compared to 35 cells per 10,000 μm^2 (ganglia areas) in the intact small intestine of mice [11].

The distribution of neurons in depth was analyzed at depths of every 20 μm. In all three groups almost all neurons were located within 100 μm of the surface (**Figure 9*A–C***). The total number of neurons in MOS-treated mice was about four-fold of that in SB plus MOS and DMSO treated mice (**Figure 9*D***).

Correctly identified fluorescent neurons by 2PM are proved to be neurons with an independent technique at the anastomotic site. NF-positive, DLX2-negative, BrdU-positive and GFP-positive cell is identified as a new neuron (**Figure 10*A–D***). NF-negative, DLX2-positive, BrdU-positive and GFP-positive cells seem to be neural progenitors. At this anastomotic site, GFAP-positive enteric glial cells are not found (**Figure 10*E***).

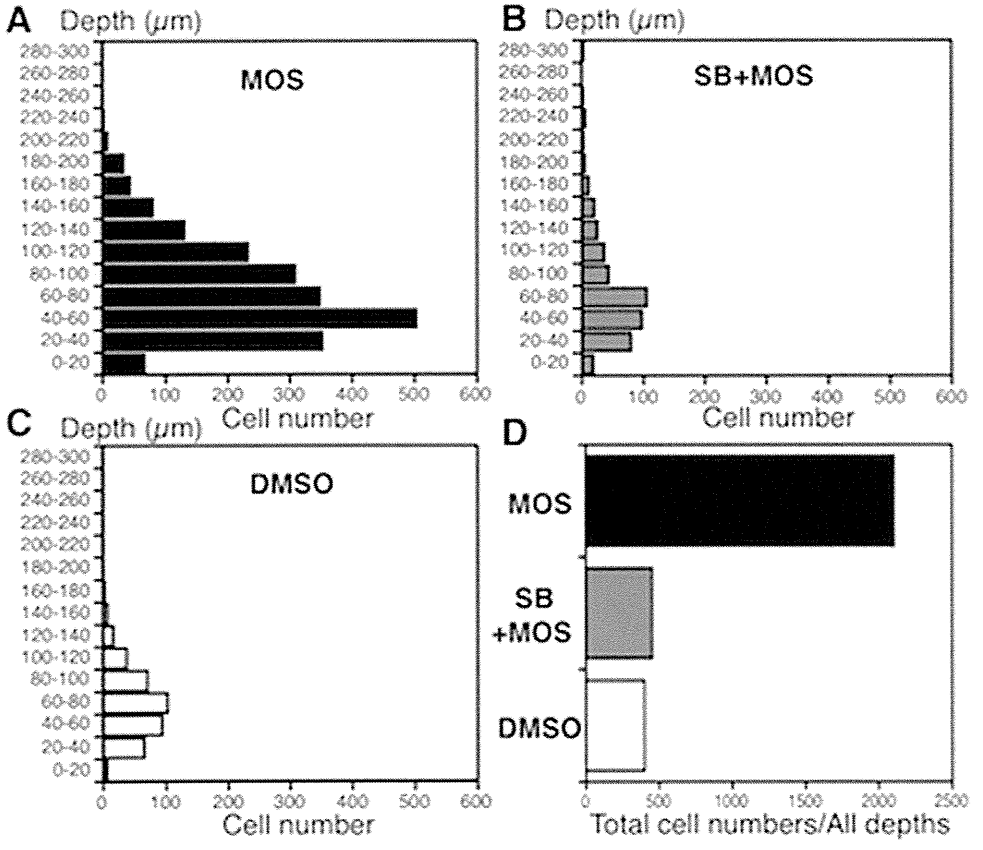

Figure 9. The distribution of total neurons in MOS (n = 5), SB+MOS (n = 4) and vehicle-treated (n = 4) mice. *A, B, C.* Number of total neurons at depths of every 20 μm. *D.* Cumulative numbers from all depths.
doi:10.1371/journal.pone.0054814.g009

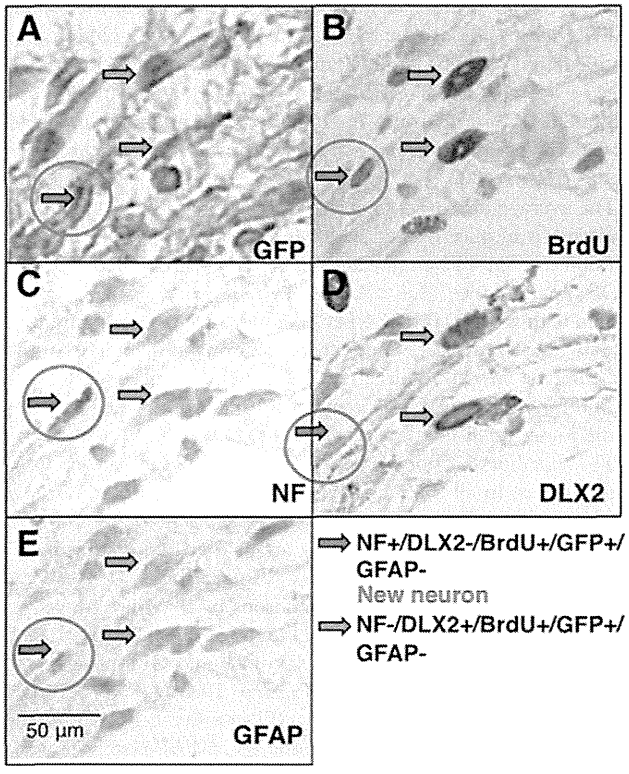

Figure 10. Correctly identified fluorescent neurons by 2PM are proved to be neurons at the anastomosis in MOS-treated mice. *A.* Green Fluorescent Protein (GFP)-positive cells. *B.* 5-bromo-2′-deoxyuridine (BrdU)-positive cells. *C.* A neural marker, neurofilament (NF)-positive cell. *D.* A neural stem cell marker, distal less homeobox 2 (DLX2)-positive cells. *E.* glial fibrillary acidic protein (GFAP)-negative cells. Red arrows indicate NF+/DLX2−/BrdU+/GFP+/GFAP- cell: this cell is a new neuron. Green arrows indicate NF−/DLX2+/BrdU+/GFP+/GFAP- cells: these cells seem to be neural progenitors. Similar results are obtained in other preparations.
doi:10.1371/journal.pone.0054814.g010

Discussion

This is the first study involving in vivo imaging of enteric neurons with 2PM, although in vivo imaging of enteric neurons with confocal laser endomicroscopy has been recently performed [9]. We detected the formation of newly generated neurons in the thick granulation tissue at the site of anastomosis. Imaging with 2 PM allowed enteric neural imaging several hundred microns deep within the gut of living mouse. In contrast to the brain tissue [7], the structure of the gut tissue is complex, consisting of multiple layers and tissue types, including mucosa, submucosa, circular and longitudinal muscles, blood vessels and crypt glands. Therefore, to enhance visualization of enteric neurons we used Thy1-GFP mice [8] after confirmation of expression of cytoplasmic GFP in enteric neurons in preliminary studies. In the present study, newly formed enteric neurons also expressed cytoplasmic GFP. In future studies, we are planning functional studies of enteric neurons using in vivo imaging with 2PM and genetically encoding calcium indicators [12].

A critical obstacle to overcome in order to obtain clear images of enteric neurons in vivo was to suppress motion disturbance associated with gut motility. Otherwise, observed images would be blurry and non-interpretable. We found that pinning and intraluminal injection of papaverine eliminated tissue movement and allowed for the acquisition of sharp images.

One week after surgical anastomosis, MOS facilitated formation of newly generated enteric neurons in the granulation tissue at the anastomosis. However, even 4 weeks after surgery, only a small number of newborn neurons were identified in the granulation tissue of vehicle-treated control animals. The effects of MOS on neurogenesis were completely antagonized by treatment with a 5-HT_4 receptor antagonist, indicating that MOS facilitated formation of newborn enteric neurons via 5-HT_4-receptor activation. Although the number of newly formed enteric neurons was significantly higher in the MOS-treated mice as compared to antagonist treated and vehicle controls, the distribution pattern of newly formed enteric neurons was similar, i.e., neurons were distributed close to the edge of the granulation tissue. This suggested the possibility that neural stem cells were mobilized from the outside of the granulation tissue.

Enteric nervous system (ENS) development is relevant to Hirschsprung's disease (HSCR; congenital aganglionosis of the terminal bowel) and related diseases, which are still imperfectly treated. It is well known that mutations in genes encoding the Ret receptor tyrosine kinase and endothelin receptor type B are involved in HSCR pathogenesis [13,14]. We found MOS increased mRNA of c-Ret receptor tyrosine kinase in a rat model and that a 5-HT_4 receptor antagonist completely blocked this effect [15]. Therefore, it seems likely that the target molecule of MOS is the Ret receptor tyrosine kinase.

Enteric neurogenesis must be strictly controlled, because hyperplasia of enteric neurons due to hypersensitivity for glial cell-derived neurotrophic factor (GDNF)-Ret signaling reversely results in HSCR [16]. Nevertheless, treatment with 5-HT_4 receptor agonists such as MOS could be a promising tool to treat HSCR and related disorders.

In conclusion, *in vivo* imaging by 2PM allowed for high-resolution deep imaging of the intestines *in vivo*. Thick granulation tissue at the site of anastomosis, including newly formed ganglion-like structures and nerve fibers, could be studied in the intact murine small intestine, whereas this would have been impossible with traditional fluorescence or confocal microscopy. The results presented here confirmed that oral administration of MOS promotes the generation of enteric neurons by activation of enteric neural 5-HT_4-receptors in the murine small intestine. The present technology would be promising for *in vivo* imaging of enteric neurons distributed throughout the entire gastrointestinal tract as a means of evaluating enteric neural function and dysfunction in the normal gut and in, for example, diabetic [17] and parkinsonism mouse models [18].

The recent publications suggest that mouse enteric glia can be neuronal precursors and thus form neurons *in vitro* and *in vivo* under specific circumstances [19–21]. Therefore, we have investigated glia and/or their relation to the newly formed "neurons". However, we did not found any enteric glial cells at the anastomotic site. It seems unlikely that enteric glial cells contribute to neurogenesis at least at the anastomotic site.

Acknowledgments

We thank Prof. Gary Mawe in the Department of Anatomy and Neurobiology in the University of Vermont for his critical reading of this manuscript.

Author Contributions

Conceived and designed the experiments: KG HK JN MT. Performed the experiments: KG GK YL HM TI. Analyzed the data: KG GK HK JN MT. Contributed reagents/materials/analysis tools: KG IK YL KO. Wrote the paper: KG MT.

References

1. Katsui R, Kojima Y, Kuniyasu H, Shimizu J, Koyama F, et al. (2008) A new possibility for repairing the anal dysfunction by promoting regeneration of the reflex pathways in the enteric nervous system. Am J Physiol Gastrointest Liver Physiol 294: G1084–G1093.
2. Yamanouchi M, Shimatani H, Kadowaki M, Yoneda S, Nakagawa T, et al. (2002) Integrative control of rectoanal reflex in guinea pigs through lumbar colonic nerves. Am J Physiol Gastrointest Liver Physiol 283: G148–G156.
3. Matsuyoshi H, Kuniyasu H, Okumura M, Misawa H, Katsui R, et al. (2010) A 5-HT_4-receptor activation-induced neural plasticity enhances in vivo reconstructs of enteric nerve circuit insult. Neurogastroenterol Motil 22: 806–e226.
4. Takaki M, Misawa H, Matsuyoshi H, Kawahara I, Goto K, et al. (2011) In vitro enhanced differentiation of neural networks in ES gut-like organ from mouse ES cells by a 5-HT_4-receptor activation. Biochem Biophys Res Commun 406: 529–533.
5. Liu M, Gershon MD (2006) Neuroprotective/trophic effects of 5-HT_4 receptor stimulation on enteric neurons of mice. Neurogastroenterol Motil 18: 780–781.
6. Liu M-T, Kuan Y-H, Wang J, Hen R, Gershon MD (2009) 5-HT_4 Receptor-mediated neuroprotection and neurogenesis in the enteric nervous system of adult mice. J Neurosci 299: 683–969.
7. Wake H, Moorhouse AJ, Jinno S, Kohsaka S, Nabekura J (2009) Resting microglia directly monitor the functional state of synapses in vivo and determine the fate of ischemic terminals. J Neurosci 29: 3974–3980.
8. Feng G, Mellor RH, Bernstein M, Keller-Peck C, Nguyen QT, et al. (2000) Imaging neuronal subsets neurotechnique in transgenic mice expressing multiple spectral variants of GFP. Neuron 28: 41–51.
9. Ohya TR, Sumiyama K, Takahashi-Fujigasaki J, Dobashi A, Saito S, et al. (2012) In vivo histologic imaging of the muscularis propria and myenteric neurons with probe-based confocal laser endomicroscopy in porcine models (with videos). Gastroinrestinal Endoscopy 75: 405–410.
10. Bharucha AE, Camilleri M, Haydock S, Ferber I, Burton D, et al. (2000) Effects of a serotonin 5-HT_4 receptor antagonist SB-207266 on gastrointestinal motor and sensory function in humans. Gut 47: 667–674.
11. Thacker M, Rivera LR, Cho H-J, Furness JB (2011) The relationship between glial distortion and neuronal changes following intestinal ischemia and reperfusion. Neurogastroenterol Motil 23: e500–e509.
12. Nakai J, Ohkura M, Imoto K (2001) A high signal-to-noise Ca^{2+} probe composed of a single green fluorescent protein. Nature Biotechnol 19: 137–141.
13. Gershon MD (2010) Developmental determinants of the independence and complexity of the enteric nervous system. Trends in Neuroscience 33: 446–456.
14. Hofstra RMW, Osinga J, Buys CHCM (1997) Mutations in Hirschsprung disease: When does a mutation contribute to the phenotype. Eur J Hum Genet 5: 180–185.
15. Kawahara I, Kuniyasu H, Matsuyoshi H, Goto K, Obata K, et al. (2012) The comparison of effects of a selective 5-HT reuptake inhibitor versus a 5-HT_4 receptor agonist on in vivo neurogenesis at the rectal anastomosis in rats. Am J Physiol Gastrointest Liver Physiol 302: G588–G597.
16. Zhou R, Niwa S, Homma N, Takei Y, Hirokawa N (2009) KIF26A is an unconventional kinesin and regulates GDNF-Ret signaling in enteric neuronal development. Cell 139: 802–813.
17. Surendran S, Kondapaka SB (2005) Altered expression of neuronal nitric oxide synthase in the duodenum longitudinal muscle-myenteric plexus of obesity induced diabetes mouse: Implicatoins on enteric neurodegeneration. Biochem Biophys Res Commun 338: 919–922.
18. Kurosaki M, Muramatsu Y, Kato H, Araki T (2004) Biochemical, behavioral and immunohistochemical alterations in MTPT-treated mouse model of Parkinson's disease. Pharmacol Biochem Behavior 78: 143–153.
19. Joseph NM, He S, Quintana E, Kim Y-G, Núñez G, et al. (2011) Enteric glia are multipotent in culture but primarily form glia in the adult rodent gut. J Clin Invest 121: 3398–3411.
20. Laranjeira C, Sandgren K, Kessaris N, Richardson W, Potocnik A, et al. (2011) Glial cells in the mouse enteric nervous system can undergo neurogenesis in response to injury. J Clin Invest 121: 3412–3424.
21. Gershon MD (2011) Behind an enteric neuron there may lie a glial cell. J Clin Invest 121: 3386–3389.

Human Pathology (2012) xx, xxx–xxx

ELSEVIER

Human PATHOLOGY

www.elsevier.com/locate/humpath

Original Contribution

Tropomyosin receptor kinases B and C are tumor progressive and metastatic marker in colorectal carcinoma☆

Tomonori Sasahira[a], Nobuhiro Ueda[b], Miyako Kurihara[a,b], Sayako Matsushima[a], Hitoshi Ohmori[a], Kiyomu Fujii[a], Ujjal K. Bhawal[a], Kazuhiko Yamamoto[b], Tadaaki Kirita[b], Hiroki Kuniyasu[a,*]

[a]*Department of Molecular Pathology, Nara Medical University School of Medicine, Kashihara, Nara 634-8521, Japan*
[b]*Department of Oral and Maxillofacial Surgery, Nara Medical University School of Medicine, Kashihara, Japan*

Received 23 May 2012; revised 25 September 2012; accepted 28 September 2012

Keywords:
Trk;
Colon cancer;
Nodal metastasis;
Peritoneal metastasis;
Liver metastasis

Summary Members of the tropomyosin receptor kinase (Trk) family have a high affinity for neurotrophins and regulate neuronal survival. The role of Trks in cancer is still controversial. The expression and role of TrkB and TrkC were examined in colorectal cancer (CRC). Immunohistochemistry analysis of TrkB and TrkC performed in 133 patients with CRC. Using human CRC cell lines, expression of vascular endothelial growth factor (VEGF) and transforming growth factor β, cell growth, invasion, and apoptosis were examined by knockdown methods. Immunohistochemistry showed positive results of TrkB and TrkC (23.3% and 12.8%, respectively). TrkB expression was associated with local progression ($P = .0284$), clinical stage ($P = .0026$), nodal metastasis ($P = .0068$), and peritoneal metastasis ($P = .0026$). TrkC expression was only related to liver metastasis ($P = .0001$). Coexpression of TrkB or TrkC and their ligands was found in 80.6% and 82.4% of cases, respectively. In vitro analysis using human CRC cells showed that TrkB positively regulated gene expression of VEGF-A ($P < .05$) and VEGF-C ($P < .05$), whereas TrkC suppressed transforming growth factor β expression ($P < .05$). TrkB and TrkC induced cell growth ($P < .05$) and invasion ($P < .05$), respectively. Both TrkB and TrkC showed antiapoptotic effect ($P < .05$). These results suggest that TrkB and TrkC have a tumor progressive function and may be a useful diagnostic and therapeutic target in CRC.

1. Introduction

Colorectal cancer (CRC) is the third most common malignancy worldwide [1] and is responsible for more than 500 000 deaths annually [2]. The overall 5-year survival rate decreases from approximately 80% in patients without nodal metastases to 50% in patients with nodal metastasis [3]; it is less than 10% in those with distant metastasis [4]. Liver metastasis is found in 30% to 60% of metastatic cases, and most patients who have liver metastases die within 5 years of diagnosis [5]. Therefore, early detection of CRC is

Abbreviation: CRC, colorectal cancer; Trk, tyrosine kinase receptor; NGF, nerve growth factor; BDNF, brain-derived neurotrophic factor; NT, neurotrophin; BMP, bone morphogenetic protein; VEGF, vascular endothelial growth factor; TGF, transforming growth factor; PI3K, phosphatidylinositol 3′-kinase; MAPK, mitogen-activated protein kinase; mTOR, mammalian target of rapamycin; MMP, matrix metalloproteinase; EMT, epithelial-mesenchymal transition.

☆ Conflict of interest statement: We declare that there is no any financial support or relationships that may pose a conflict of interest in the contents of the submitted manuscript.

* Corresponding author. Department of Molecular Pathology, Nara Medical University, 840 Shijo-cho, Kashihara, Nara 634-8521, Japan.
E-mail address: cooninh@zb4.so-net.ne.jp (H. Kuniyasu).

0046-8177/$ – see front matter © 2012 Published by Elsevier Inc.
http://dx.doi.org/10.1016/j.humpath.2012.09.016

important, and elucidation of a detailed molecular mechanism of an organization promoting metastasis of CRC is critical.

Ligands for the tropomyosin receptor kinase (Trk) family are neurotrophins (NTs); TrkA binds to nerve growth factor, TrkB binds to brain-derived neurotrophic factor (BDNF) and NT-4/5, and TrkC binds to NT-3 [6,7]. NTs initiate autophosphorylation at the extracellular domain of Trks by binding to Trks and promoting downstream signaling transduction pathways [7]. The Trk family has been reported as regulating neuronal survival and differentiation [8]. Trks also act as oncogenes; TrkA overexpression has been observed in thyroid carcinoma [9,10]. Higher expression levels of TrkB have been found in many tumors and are associated with more aggressive tumor behavior [11,12]. In CRC, TrkC directly binds to the bone morphogenetic protein type II receptor and inhibits bone morphogenetic protein signaling [13]. Moreover, TrkB and TrkC inhibit apoptosis in ovarian cancer and neuroblastoma cells via phosphatidylinositol 3′-kinase (PI3K)–AKT signaling, respectively [14,15]. However, it has been reported that TrkB expression is down-regulated in prostate cancer [16]. Furthermore, TrkC plays an favorable role in medulloblastoma, leading to a good clinical outcome [17], and cases of neuroblastoma with high expression of TrkA or TrkC have a better prognosis [18,19]; thus, the role of Trks in tumors is still controversial.

It has been reported recently that TrkB induces angiogenesis by activation of vascular endothelial growth factor (VEGF)-A in neuroblastoma [20] and that TrkC suppresses transforming growth factor (TGF) β signaling in breast cancer [21]. We also confirmed that TrkB and TrkC promote tumor progression, nodal metastasis, and induction of angiogenesis and lymphangiogenesis in oral cancer [22]; however, not much information is available about the expression pattern and clinicopathologic significance of Trks in CRC. In this study, we examined the expression of TrkB/C and the effects on the VEGF family and TGF-β signaling by using clinical samples and cell lines of CRC.

2. Materials and methods

2.1. Tissue samples

Formalin-fixed, paraffin-embedded 133 cases of primary CRCs (92 men and 41 woman; age range, 48-79 years; means, 68.7 years), and each 9 fresh-frozen specimens of CRC and noncancerous colorectal mucosa were randomly selected from Nara Medical University Hospital, Kashihara, Japan, and Miyoshi General Hospital, Miyoshi, Japan. All cases were not to operate preoperative treatment. Tumor staging and the histology of CRCs are classified according to TNM classification and World Health Organization classification, respectively. Medical records and prognostic follow-up data were obtained from the patient database managed by the hospital. Because written informed consent was not obtained, identifying information for all samples was removed before analysis for strict privacy protection; the procedure was in accordance with the Ethical Guidelines for Human Genome/Gene Research enacted by the Japanese Government.

2.2. Immunohistochemistry

Consecutive 3-μm sections were cut from each block, and immunohistochemical analysis was performed as we described previously [23,24]. An immunoperoxidase technique was done after antigen retrieval with microwave treatment (95°C) in citrate buffer (pH 6.0) for 45 minutes or pepsin (DAKO, Carpinteria, CA) treatment for 20 minutes. After endogenous peroxidase block by 3% H_2O_2-methanol for 15 minutes, specimens were rinsed with phosphate-buffered saline (PBS) 3 times. Anti-TrkB anti-TrkC antibody (Santa Cruz Biotechnology, Santa Cruz, CA), anti-BDNF antibody (R&D Systems, Temecula, CA), and anti–NT-3 antibody (CHEMICON, Minneapollis, MN), diluted by 0.5 μg/mL were used for primary antibody. After a 12-hour incubation at room temperature, specimens were rinsed with PBS 3 times and treated for an hour at room temperature with the secondary antibody peroxidase-conjugated antimouse or antirabbit antibody (MBL, Nagoya, Japan) diluted at 0.5%. The specimens were then rinsed with PBS 3 times and color developed with diaminobenzidine (DAB) solution (DAKO). After washing, specimens were counterstained with Meyer hematoxylin (Sigma Chemical, St Louis, MO). Immunostaining of all samples was performed at the same conditions of antibody reaction and DAB exposure. For evaluation of Trks expression, we observed 20 microscopic fields at 100-fold magnification. Immunoreactivity of Trks was classified according to Allred score (AS) [25]. We divided the immunoreactivity into 4 grades by AS; grade 0, AS is 0; grade 1, AS is 2 to 4; grade 2, AS is 5 to 6; and grade 3, AS is 7 to 8. Cases with grade 2 to 3 staining were defined as TrkB or TrkC positive [23,24,26].

2.3. Cell culture

Human CRC cell lines, WiDr, Colo320, HT29, and LoVo cells were obtained from Health Science Research Resources Bank and maintained in Dulbbeco modified Eagle medium (Wako Pure Chemical, Osaka, Japan) supplemented with 10% fetal bovine serum (Sigma Chemical) under the conditions of 5% CO_2 in air at 37°C.

2.4. Quantitative reverse transcription–polymerase chain reaction

Total RNA was extracted using RNeasy Mini Kit (Qiagen, Valencia, CA) and total RNA (1 μg) was synthesized with the ReverTra Ace qRT Kit (Toyobo, Osaka, Japan). Quantitative

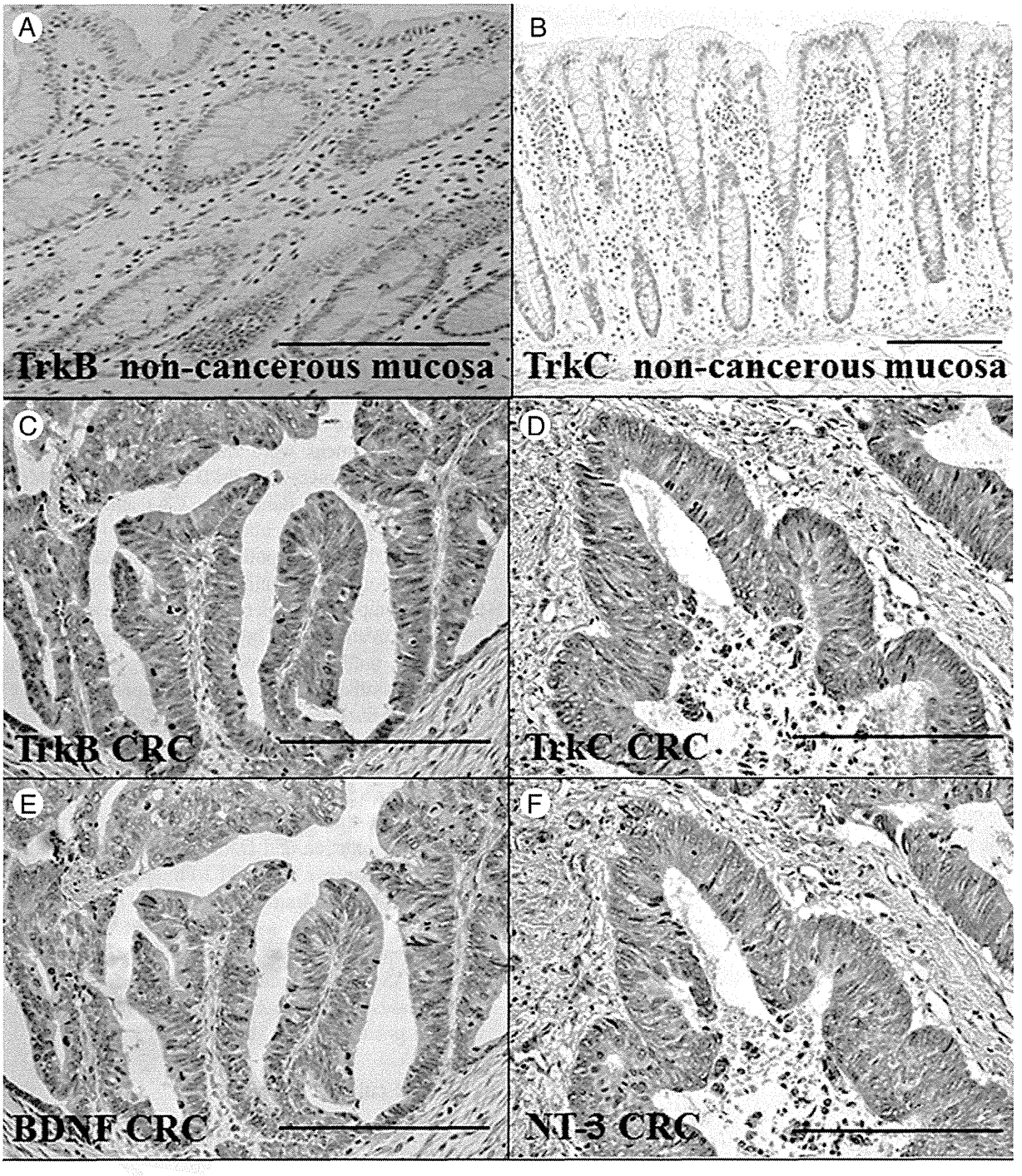

Fig. 1 Immunohistochemistry of TrkB, TrkC, BDNF, and NT-3. No expression of TrkB (A) and TrkC (B) was observed in normal colorectal mucosa. Cytoplasmic expression of TrkB (C) in a patient with nodal and peritoneal metastasis–positive CRC and TrkC expression (D) in a patient with liver metastasis–positive CRC. BDNF (E) and NT-3 (F) expression cases with TrkB- and TrkC-positive CRC, respectively. Bar, 100 μm.

reverse transcription–polymerase chain reaction (PCR) were performed on StepOne Plus Real-Time PCR Systems (Applied Biosystems, Foster City, CA) using TaqMan Fast Universal PCR Master Mix (Applied) and analyze the relative standard curve quantification method. PCR condition was according to the manufacturer's instructions and GAPDH messenger RNA (mRNA) level was amplified for internal control. TaqMan Gene Expression Assays of TrkB, TrkC, VEGF-A, VEGF-C, VEGF-D, TGF-β, mitogen-activated protein kinase (MAPK) 14 (MAPK p38), PIK3CA (PI3K), AKT1, mammalian target of rapamycin (MTOR), and matrix metalloproteinase (MMP)-2, MMP-9, and GAPDH were purchased from Applied

Biosystems. PCR products were electrophoresed on 2% agarose gel, and all PCRs were done at triplicate.

2.5. Small interfering RNA

Stealth Select RNAi (siRNA) for TrkB and TrkC were purchased from Invitrogen (Carlsbad, CA). AllStars Negative Control siRNA was used for control (Qiagen). Twenty nanometers of siRNA was transfected with Lipofectamine 2000 (Invitrogen) according to the provider's recommendations.

Table 1 Relationship between Trk expression and clinicopathologic parameters

Parameters	TrkB		TrkC	
	−	+	−	+
Sex				
Male	70	22	81	11
Female	32	9	35	6
P	NS		NS	
Age (y)				
≤60	37	11	40	8
>60	65	20	76	9
P	NS		NS	
Histologic differentiation [a]				
Well	42	15	50	7
Mod, Por, Muc	60	16	66	10
P	NS		NS	
T classification				
Tis-T2	32	4	34	2
T3-T4	70	27	82	15
P	NS		NS	
T classification				
Tis-T3	92	23	101	14
T4	10	8	15	3
P	.0284		NS	
Clinical stage				
I, II	64	10	68	6
III, IV	38	21	48	11
P	.0026		NS	
Nodal metastasis				
Negative	64	11	68	7
Positive	38	20	48	10
P	.0068		NS	
Peritoneal metastasis				
Negative	101	26	115	12
Positive	1	5	1	5
P	.0026		NS	
Liver metastasis				
Negative	98	29	115	12
Positive	4	2	1	5
P	NS		.0001	

NOTE. Relationship between expression of Trks and clinicopathologic parameters were calculated by Fisher exact *t* test. T classification and clinical stage were classified according to the TNM classification.

Abbreviations: NS, not significant.

[a] Histologic differentiation: well, well-differentiated adenocarcinoma; Mod, moderately differentiated adenocarcinoma; Por, poorly differentiated adenocarcinoma; Muc, mucinous carcinoma.

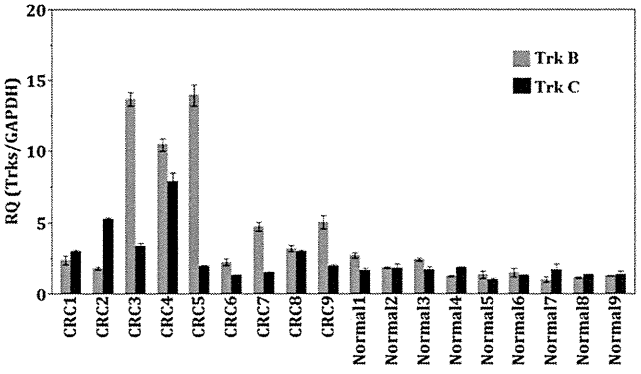

Fig. 2 Gene expression of TrkB and TrkC in CRC and normal colorectal mucosa. Error bars, SD.

2.6. Cell growth assay

The cells were seeded at density of 2000 cells per well of 96-well tissue culture plates and incubated for 48 hours at 37°C. Cell growth was assessed by MTT assay using the incorporation of 3-(4,5-dimethylthiazol-2-yl)-2,5-diphenyl-tetrazolium bromide (Sigma Chemical). The experiments were performed in triplicate.

2.7. In vitro invasion assay

A modified Boyden chamber assay was performed using the BD BioCoat Cell Culture Inserts glued to type IV collagen (Becton-Dickinson, Bedford, MA) as described previously. Cells were suspended in 500 μL of Dulbbeco modified Eagle medium and placed 4 in the insert. After a 48-hour incubation at 37°C, the filters were stained with hematoxylin. The stained cells were counted in whole inserts at ×100 magnification. Each experiment was repeated at least 3 times.

2.8. Apoptotic assay

Apoptotic cells were detected by the terminal deoxynucleotidyl trsnsferase (TdT)-mediated dUTP-biotin nick and labeling (TUNEL) assay using the In Situ Cell Death Detection Kit, POD (Roche Diagnostics, Indianapolis, IN) according to the manufacturer's protocol. The experiments were performed in triplicate.

2.9. Immunocytochemistry

The cells grown in a monolayer on the glass slides were fixed for 12 hours with 10% buffered formalin at 4°C. The cells were immunostained with anti–Ki-67 antibody (DAKO). Peroxidase-conjugated secondary antibody and DAB were used for detection. For the counterstaining, Meyer hematoxylin was used. For evaluation of HuD expression, we observed 20 microscopic fields at 200-fold magnification and we counted tumor cells per case, and the results were

expressed as percentage of tumor cells with positive nuclei and these values were defined as HuD labeling index.

2.10. Statistical analysis

Statistical analysis was performed with JMP8 (SAS Institute, Cary, NC). Statistical differentiation was calculated with Fisher exact probability test and Student *t* test. *P* values less than .05 were regarded as statistically significant.

3. Results

3.1. Expression of Trks in patients with CRC

At first, we performed immunohistochemistry analysis of TrkB and TrkC in 133 patients with CRC. Expression of TrkB (Fig. 1A) and TrkC (Fig. 1B) was negative or very weak in nontumoral colorectal mucosa; immunoreactivity of TrkB (Fig. 1C) and TrkC (Fig. 1D) was localized to the cytoplasm of CRC cells. Of the 133 patients with CRC, expression of TrkB and TrkC was found in 31 (23.3%) and 17 (12.8%) patients, respectively. The relationship between expression of TrkB or TrkC and clinicopathologic parameters is summarized in Table 1. Expression of TrkB was significantly associated with clinical stage ($P = .0026$). Of the 59 patients with advanced-stage disease (stages III and IV), 21 (35.6%) patients showed TrkB expression. However, in the 74 patients with early-stage CRC (stages I and II), only 10 (13.5%) patients showed TrkB expression. With respect to local progression of the tumor (T factor), no relationship was observed when the cases were divided into 2 groups—one including Tis to T2 cases and the other, T3 and T4 cases—but expression of TrkB in T4 patients (8/18; 44.4%) was higher than that in other patients (23/115; 20%) ($P = .0284$). In patients with nodal metastasis or peritoneal dissemination, TrkB expression was found to be 34.5% (20/58) or 83.3% (5/6), respectively, whereas immunoreactivity of TrkB was observed in patients with no nodal progression (11/75; 14.7%) or peritoneal metastasis (26/127; 20.5%) ($P = .0068$ and $P = .0026$, respectively). On the other hand, TrkC expression only correlated with liver metastasis, and 5 (83.3%) of 6 patients with liver metastasis showed TrkC immunopositivity ($P = .0001$). Twenty-five (80.6%) of 31 and 14 (82.4%) of 17 patients showed coexpression of TrkB/BDNF (Fig. 1E) and TrkC/NT-3 (Fig. 1F), respectively. No relationship was found between TrkB or TrkC expression and other clinicopathologic characteristics of CRC. We also validated that TrkA expression levels were comparable in

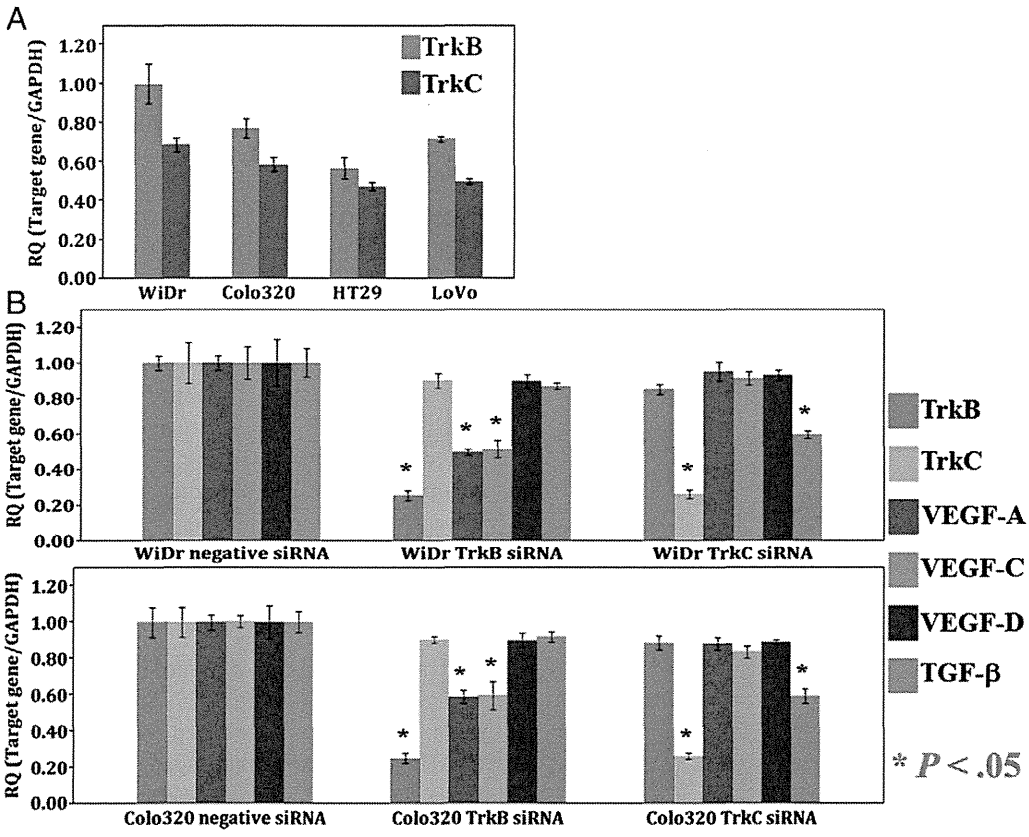

Fig. 3 A, TrkB and TrkC mRNA expression in WiDr and Colo320 CRC cells. B, Effect on gene expression of VEGF-A, VEGF-C, VEGF-D, and TGF-β by TrkB or TrkC siRNA treatment in WiDr and Colo320 CRC cells. Error bars, SD.

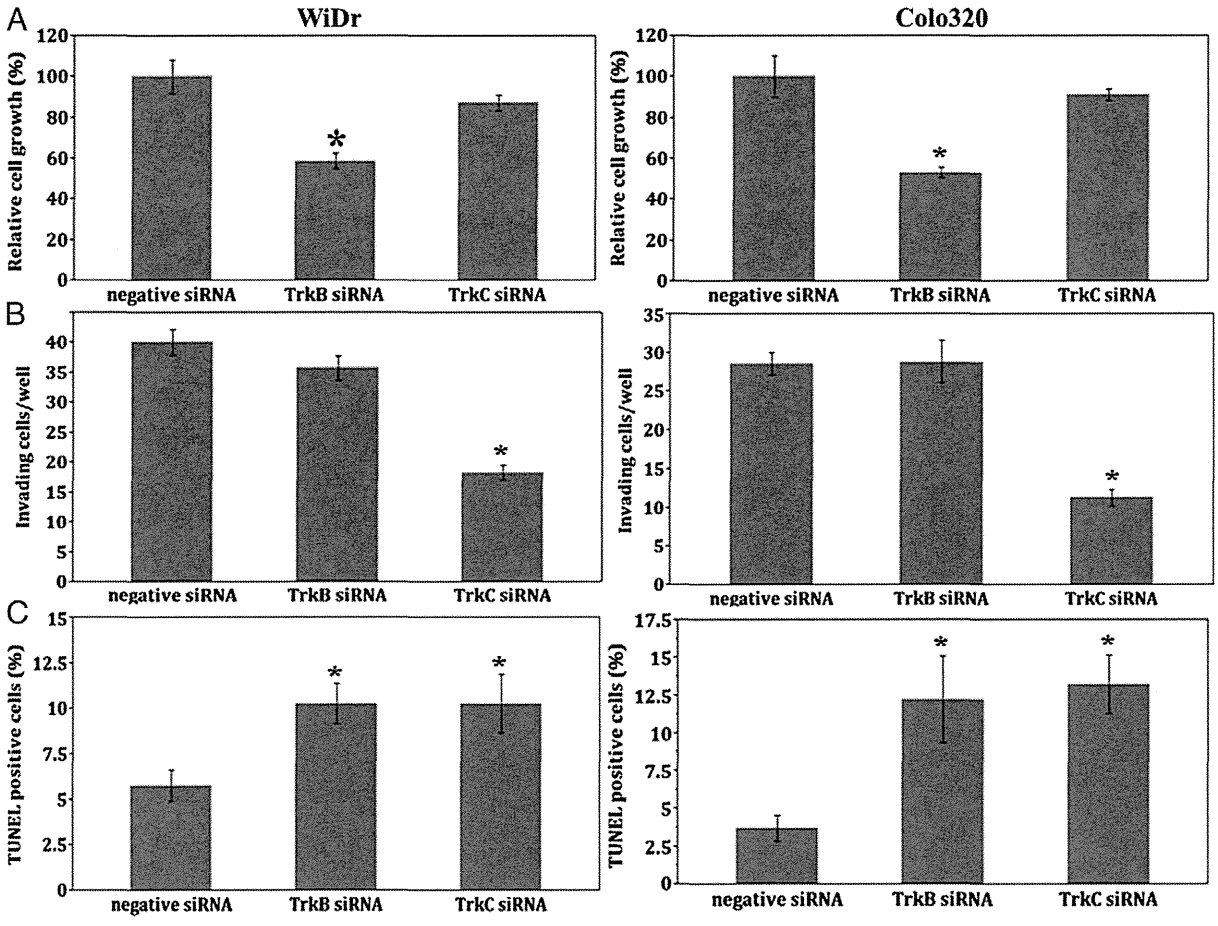

Fig. 4 Effect on cell growth ability (A), invasion ability (B), number of TUNEL-positive cells (C), and activation of caspase-3 in WiDr and Colo320 CRC cells. Error bars, SD. *$P < .05$.

colon cancer specimens (data not shown). We next examined mRNA expression of TrkB and TrkC in 9 samples each of CRC and noncancerous colorectal mucosa by quantitative reverse transcription PCR. TrkB ($P < .05$) and TrkC ($P < .05$) were up-regulated to a greater extent in the CRC samples than in noncancerous colorectal mucosa samples (Fig. 2).

3.2. Gene expression analysis of CRC cells

Human CRC–derived WiDr and Colo320 cells were expressed higher in TrkB and TrkC than in other cells, and therefore, we performed another analysis using WiDr and Colo320 cells (Fig. 3A). Because recent reports suggested that TrkB induces VEGF-A activity (20) and that TrkC inhibits TGF-β signaling (21), we further confirmed changes in VEGF-A, VEGF-C, VEGF-D, and TGF-β expression levels with TrkB or TrkC siRNA treatment in both cell types. Gene knockdown of TrkB decreased VEGF-A and VEGF-C expression. No change of VEGF-D and TGF-β expression was observed with TrkB siRNA treatment. After treatment with TrkC siRNA, only down-regulation of TGF-β signaling was detected, and the expression level of the VEGF family did not change in either cell type (Fig. 3B).

3.3. Functional analysis of TrkB and TrkC in CRC cells

We next investigated cell growth, invasiveness, and apoptotic ability, as influenced by TrkB or TrkC siRNA treatment in WiDr and Colo320 cells. Cells treated with TrkB siRNA showed inhibited growth compared with those treated with negative siRNA, whereas cell growth in cells treated with TrkC siRNA did not differ from those treated with negative siRNA, in either cell line (Fig. 4A). Although the number of invading CRC cells decreased by treatment with TrkC siRNA compared with cells treated with negative siRNA, TrkB siRNA did not affect the invasive ability in CRC cells (Fig. 4B). With regard to the relationship between TrkB or TrkC and apoptosis, the number of TUNEL-positive cells increased with both TrkB siRNA–treated and TrkC siRNA–treated WiDr and Colo320 cells compared with those treated with negative siRNA (Fig. 4C).

Finally, we examined the expression of downstream target of Trk signaling such as MAPK p38 and PI3K-AKT pathways. We also confirmed MMP-2/9 expression levels and immunopositivity of Ki-67 by TrkB or TrkC knockdown treatment (Fig. 5). The expression levels of PI3K (PIK3CA)

and AKT1 were down-regulated in TrkB and TrkC siRNA treated CRC cells (Fig. 5A). The mTOR is activated by PI3K-AKT signaling [27], and mTOR expression was also reduced by TrkB and TrkC knockdown treatment (Fig. 5A). Although inhibition of MAPK14 (MAPK p38) was observed by TrkB siRNA treatment, reduction of MMP-2/9 and Ki-67 labeling index were found only in TrkC knockdown–treated CRC cells (Fig. 5A, B). Above all, results suggested that TrkB and TrkC act as tumor progressive factors, although their functional roles in human CRC differ.

4. Discussion

Trks have high affinity for NTs; they regulate the survival and differentiation of developmental neurons and maintain growth and action of neuronal synapses throughout adulthood [28]. Trks are regarded as oncogenes [11–15,20,21], and we recently found that TrkB and TrkC have tumor progressive functions in oral squamous cell carcinoma [22]. However, it has been reported that Trks have tumor suppressive functions; thus, the role of Trks in cancer remains controversial. In this study, we investigated the expression and functional role of TrkB and TrkC in CRC. CRC specimens showed higher mRNA expression of TrkB and TrkC than did noncancerous colorectal mucosa. TrkB and TrkC are receptors for BDNF and NT-3 [6,7], respectively, and coexpression of TrkB/BDNF and TrkC/NT-3 was observed in many CRC specimens, with both Trks being positive. Recent studies have shown that TrkB and TrkC are involved in anticancer drug resistance by depression of apoptosis through production of PI3K-AKT signaling activity [14,15]. Restoration of apoptosis and inhibition of PI3K and AKT were observed in TrkB or TrkC siRNA–treated CRC cells, and our results were consistent with those of previous reports. We also found that mTOR, which is activated by PI3K-AKT signaling [27], is regulated by TrkB and TrkC in CRC cells. The PI3K-AKT-mTOR pathways are pivotal signaling of Trks in CRC.

Although previous reports have shown that TrkB is down-regulated in prostate cancer [16], high expression of TrkB is strongly correlated with local progression of tumor (T grade), clinical stage, nodal metastasis, and peritoneal metastasis in CRC. Nakamura and colleagues [20] showed that TrkB regulates VEGF-A expression in neuroblastoma. Our present data are congruent with their report, and we discovered that TrkB also up-regulated VEGF-C activity. It is generally accepted that VEGF-A and VEGF-C trigger tumoral angiogenesis and lymphangiogenesis, respectively [29].

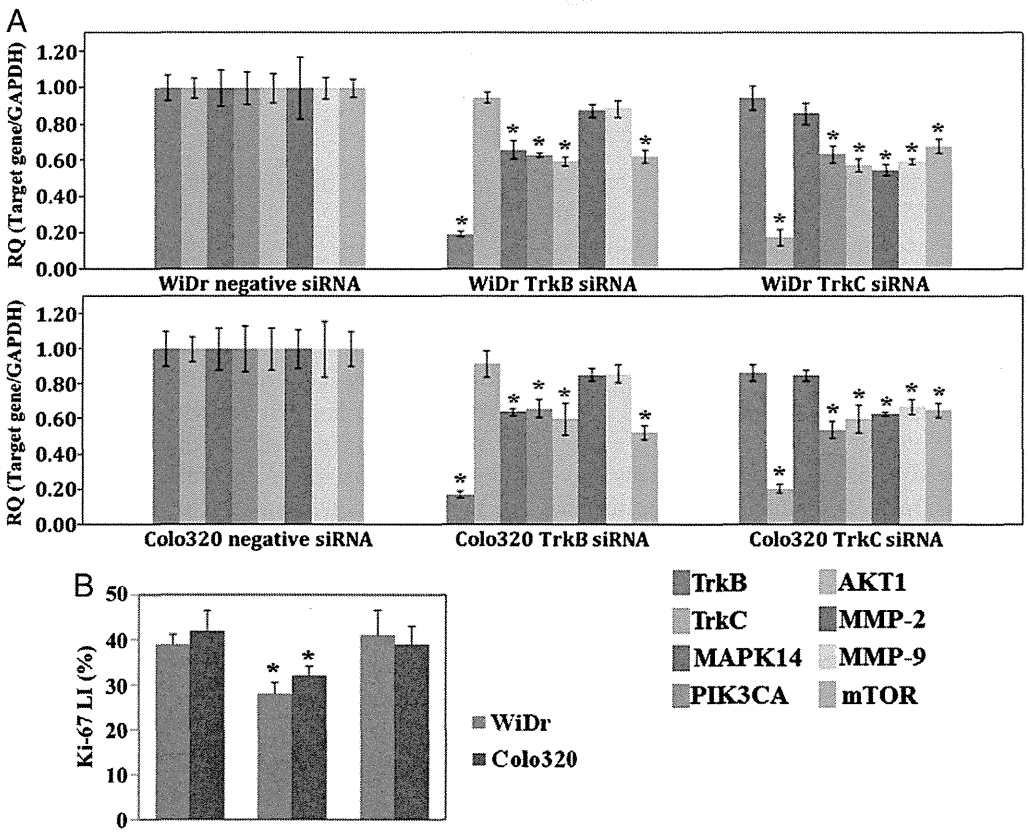

Fig. 5 A, Expression levels of MAPK14, PIK3CA, AKT1, MMP-2, MMP-9, and mTOR by TrkB or TrkC siRNA treatment in WiDr and Colo320 cells. B, Ki-67 Li in TrkB or TrkC siRNA–treated WiDr and Colo320 cells. Error bars, SD. *$P < .05$.

We have previously shown that both VEGF-A and VEGF-C can significantly induce angiogenesis and lymphangiogenesis and consequently promote tumor progression and nodal metastasis [24]. Furthermore, our recent studies showed that TrkB accelerates angiogenesis and lymphangiogenesis of oral squamous cell carcinoma [22]. TrkB may be a positive regulator of tumor progression and metastasis, possibly through activation of VEGF-A and VEGF-C. We also confirmed TrkB promotes cell growth of CRC cells by regulating of MAPK p38. Further examination will be necessary about the functional role of TrkB in CRC.

TrkC also acts as an oncogene in cutaneous carcinoma [30]. However, TrkC plays a favorable role in medulloblastoma [17] and neuroblastoma, and cases with high expression of TrkC have a better prognosis [19]; thus, the detailed role of TrkC in cancer is still controversial. In our study, we found that TrkC expression was only associated with liver metastasis and increased invasive ability of CRC. MMP-2 and MMP-9 make a basal membrane disintegrate and one of the key factors in the invasion of the cancer cells [26]. We previously reported that TrkC is regulated secretion of MMP-2/9 from oral cancer cells [22], and the present results suggested that MMP-2/9 are also associated with invasion of CRC cells. It has been reported that TrkC plays an important role in the suppression of TGF-β signaling in breast cancer [21]; however, down-regulation of TGF-β was found in TrkC knockdown–treated CRC cells. Although many reports indicate that TGF-β has tumor suppressive functions [31,32], TGF-β signaling can act as a tumor promoter by induction of epithelial-mesenchymal transition and angiogenesis or may act as a tumor suppressor [33]. Moreover, TGF-β is accelerated proliferation and invasion of CRC cells [34] and associated with tumor progression of human CRC [35]. Thus, TGF-β signaling in malignancies is more complex. The detailed relationship between TrkC and TGF-β signaling needs to be accurately elucidated, and further studies are warranted.

In conclusion, we clarified that TrkB and TrkC promote tumor progression and metastasis by an increase in cell growth or invasive ability and that they inhibit apoptosis in CRC. We also found that TrkB and TrkC regulate gene expression of VEGF-A/C and TGF-β or MMP-2/9, respectively. Our present results suggest that inhibition of TrkB and TrkC signals might be a useful therapeutic target in CRC. An appropriate animal experiment will be needed to examine this possibility further; we must confirm whether TrkB and TrkC are useful targets for molecular diagnosis and anticancer therapy in CRC.

Acknowledgment

This work was supported, in part, by Grant-in-Aid for Scientific Research from Japan Society for the Promotion of Science, Japan.

References

[1] Weitz J, Koch M, Debus J, Hohler T, Galle PR, Buchler MW. Colorectal cancer. Lancet 2005;365:153-65.
[2] Parkin DM, Bray F, Ferlay J, Pisani P. Global cancer statistics, 2002. CA Cancer J Clin 2005;55:74-108.
[3] Lee HY, Choi HJ, Park KJ, et al. Prognostic significance of metastatic lymph node ratio in node-positive colon carcinoma. Ann Surg Oncol 2007;14:1712-7.
[4] O'Connell JB, Maggard MA, Ko CY. Colon cancer survival rates with the new American Joint Committee on Cancer sixth edition staging. J Natl Cancer Inst 2004;96:1420-5.
[5] Halama N, Michel S, Kloor M, et al. Localization and density of immune cells in the invasive margin of human colorectal cancer liver metastases are prognostic for response to chemotherapy. Cancer Res 2011;71:5670-7.
[6] Thiele CJ, Li Z, McKee AE. On Trk—the TrkB signal transduction pathway is an increasingly important target in cancer biology. Clin Cancer Res 2009;15:5962-7.
[7] Jin W, Lee JJ, Kim MS, Son BH, Cho YK, Kim HP. DNA methylation-dependent regulation of TrkA, TrkB, and TrkC genes in human hepatocellular carcinoma. Biochem Biophys Res Commun 2011;406:89-95.
[8] Coppola V, Barrick CA, Southon EA, et al. Ablation of TrkA function in the immune system causes B cell abnormalities. Development 2004;131:5185-95.
[9] McGregor LM, McCune BK, Graff JR, et al. Roles of trk family neurotrophin receptors in medullary thyroid carcinoma development and progression. Proc Natl Acad Sci U S A 1999;96:4540-5.
[10] Musholt TJ, Brehm C, Hanack J, von Wasielewski R, Musholt PB. Identification of differentially expressed genes in papillary thyroid carcinomas with and without rearrangements of the tyrosine kinase receptors RET and/or NTRK1. J Surg Res 2006;131:15-25.
[11] Nakagawara A, Azar CG, Scavarda NJ, Brodeur GM. Expression and function of TRK-B and BDNF in human neuroblastomas. Mol Cell Biol 1994;14:759-67.
[12] Sclabas GM, Fujioka S, Schmidt C, et al. Overexpression of tropomysin-related kinase B in metastatic human pancreatic cancer cells. Clin Cancer Res 2005;11:440-9.
[13] Jin W, Yun C, Kim HS, Kim SJ. TrkC binds to the bone morphogenetic protein type II receptor to suppress bone morphogenetic protein signaling. Cancer Res 2007;67:9869-77.
[14] Yu X, Liu L, Cai B, He Y, Wan X. Suppression of anoikis by the neurotrophic receptor TrkB in human ovarian cancer. Cancer Sci 2008;99:543-52.
[15] Bouzas-Rodriguez J, Cabrera JR, Delloye-Bourgeois C, et al. Neurotrophin-3 production promotes human neuroblastoma cell survival by inhibiting TrkC-induced apoptosis. J Clin Invest 2010;120:850-8.
[16] Satoh F, Mimata H, Nomura T, et al. Autocrine expression of neurotrophins and their receptors in prostate cancer. Int J Urol 2001;8: S28-34.
[17] Segal RA, Goumnerova LC, Kwon YK, Stiles CD, Pomeroy SL. Expression of the neurotrophin receptor TrkC is linked to a favorable outcome in medulloblastoma. Proc Natl Acad Sci U S A 1994;91: 12867-71.
[18] Nakagawara A, Arima-Nakagawara M, Scavarda NJ, Azar CG, Cantor AB, Brodeur GM. Association between high levels of expression of the TRK gene and favorable outcome in human neuroblastoma. N Engl J Med 1993;328:847-54.
[19] Yamashiro DJ, Liu XG, Lee CP, et al. Expression and function of Trk-C in favourable human neuroblastomas. Eur J Cancer 1997;33:2054-7.
[20] Nakamura K, Martin KC, Jackson JK, Beppu K, Woo CW, Thiele CJ. Brain-derived neurotrophic factor activation of TrkB induces vascular endothelial growth factor expression via hypoxia-inducible factor-1alpha in neuroblastoma cells. Cancer Res 2006;66:4249-55.